High-order Scharfetter-Gummel-based schemes and applications to gas discharge modeling

Tuan Dung Nguyen, Christophe Besse, François Rogier

High-order Scharfetter-Gummel-based schemes and applications to gas discharge modeling

Nguyen Tuan Dung[a,b,*], Christophe Besse[b], François Rogier[a]

[a] *ONERA–The French Aerospace Lab, Toulouse 31055, France*
[b] *Institut de Mathématiques de Toulouse, UMR5219, Université de Toulouse, CNRS, UPS, F-31062 Toulouse Cedex 9, France*

Abstract

A generalized Scharfetter-Gummel method is proposed to construct the numerical flux for one-dimensional drift-diffusion equations. Instead of taking a constant approximation of the flux as Scharfetter and Gummel did in [1], we consider a p-degree polynomial with $p \geq 1$. The high order moments of the approximating flux function serve as intermediaries to bring numerical correction to the Scharfetter-Gummel flux, that the other end turns out to be the solution derivatives. Therefore, local solution reconstructions are required. The resulting schemes are high order and discretize at the same time the convective and diffusive fluxes without having to employ separately different methods to do so. The new schemes with $p = 1$ and $p = 2$ are employed to simulate atmospheric pressure discharge where they are applied to the continuity equations for electrons and ions, and solved simultaneously with Poisson's equation. Numerical results indicate that our method are robust and highly accurate.

Keywords: Atmospheric pressure discharge, Drift-diffusion equation, Scharfetter-Gummel, Finite volume method, High-order schemes, Reconstruction

1. Introduction

In this article, we introduce a new family of high-order Scharfetter-Gummel-based schemes for one-dimensional linear drift-diffusion equations. The main objective is to generalize the method put forward by Scharfetter and Gummel [1] to numerically approximate the density flux. The idea is to find a polynomial approximation of arbitrary degree p of the flux such that it is locally and quasi exact for a certain exponential function as we shall see. We take interest in discretizing the following equation,

$$\partial_t \rho + \partial_x j = 0, \quad (t, x) \in (0, T) \times \Omega, \tag{1}$$

*Corresponding author
Email address: tuan_dung.nguyen@onera.fr (Nguyen Tuan Dung)

where the density flux is defined as,

$$j = u\rho - D\partial_x\rho, \tag{2}$$

and ρ is, for example, the density of a certain substance or mixture; u, D are resp. the drift velocity and the diffusion rate; ∂_t, ∂_x denote resp. the partial derivatives in time, space; and $T > 0$ is the final time while Ω is an open bounded interval of $\mathbb{R}$.

Supposing that D is nonzero on a segment $(x_0, x_1) \subset \Omega$, we have, with $\varphi(x) = -\int_{x_0}^{x} u(s)/D(s)\mathrm{d}s$, $x \in (x_0, x_1)$,

$$j = -D\mathrm{e}^{-\varphi}(\rho\mathrm{e}^{\varphi}). \tag{3}$$

It is well known that the Scharfetter-Gummel flux is derived by taking a constant approximation J of j in (3), replacing u, D by their constant approximations $\bar{u}$, $\bar{D}$ and solving the two-point boundary problem that includes (2) and the boundary conditions $\rho(x_0) = a, \rho(x_1) = b$ for certain $a, b \in \mathbb{R}$. The resulting J equals zero if we take $\rho = \mathrm{e}^{-\bar{\varphi}}$ where $\bar{\varphi}(x) = -\bar{u}x/\bar{D}$. For this reason, the numerical flux J is locally (on (x_0, x_1)) and quasi (since $\bar{\varphi}$ is a local approximation of φ) exact for the function $\rho = \mathrm{e}^{-\varphi}$. The true flux j is of course, from (3), exact for this function. The main key of this article is to replace j in (3) with a p-degree polynomial J, instead of a constant, and follow a recursive procedure to build a new scheme that is also locally and quasi exact for the function $\mathrm{e}^{-\varphi}$. Thus the Scharfetter-Gummel scheme is a member of a new, more generic family of numerical schemes. The construction of this family will be elaborated in the next section.

The drift-diffusion equations are widely present in many numerical models for semiconductors and gas discharge. For space discretization (not necessary in one-dimension) there are a wide literature available in many classes of numerical methods, such as finite difference, finite element, finite volume, discontinuous Galerkin or spectral methods. We only mention a few that fall into the finite volume category. The most classical method is suggested by Eymard et al. [2], who used the first-order upwind scheme for the convective part and the central difference scheme for the diffusive part. A more accurate alternative is the use of the MUSCL technique that bases on the cell-wise linear reconstruction of the numerical solution and the afterward limiting of the slopes, for the convective part. There is actually a very large research on high-accuracy methods to approximate the convective flux. The aforementioned MUSCL technique was put forth by Van Leer in his pioneer series of papers [3, 4, 5, 6, 7], with the use of a slope limiter to ensure stability. Sweby [8], Harten [9] and others later studied more on a specific class of limiters that emerged as the TVD (Total Variation Diminishing) schemes. Colella and Woodward [10] extended the reconstruction to quadratic in their PPM algorithm. Later on, Harten et al. [11, 12] developed new schemes free of Gibbs phenomenon and total variation stable. Their work paved the way for the still on-going study of the ENO/WENO and related schemes (see [13] and the references therein). Further developments on arbitrary order reconstruction can be found in, for example [14] for least-squares reconstruction, or [15] for iterative reconstruction. Such high-order schemes suffer spurious oscillations in the presence of discontinuities or even gradient layers. In the authors' knowledge there is nowadays no unified framework for the limiting techniques in the same manner as MUSCL. Some attempts have

been made, such as in [16]. Such techniques are dubbed *a priori* limitations, since the corrections on the solution are made before advancing in time. Their counterparts are the *a posteriori* limitation techniques, an example of which is the MOOD method [17], that allows the advance in time with a high-order reconstruction of the solution and then a recomputing on trouble cells with lower-order reconstruction. The development of high-accuracy methods that include the diffusive flux are less emphasized though. We refer to [18] for the discussion on this subject and the elaboration of the related schemes.

Another family of numerical methods for the drift-diffusion equations is *exponentially fitted* schemes. Allen and Southwell [19] and Il'in [20] introduced a finite difference scheme that solves exactly the stationary drift-diffusion equations with constant coefficients, meaning that the discrete solution fits the (exponential) solution of the differential equation on grid points. Scharfetter and Gummel [1] introduced in the same year as Il'in a difference scheme which is based on the locally integration of the flux (2). Although the approaches ended up at the same scheme, the philosophy is different. Since the latter approach facilitates the construction of a finite volume scheme, we prefer the name Scharfetter-Gummel (SG) to refer to the scheme. The SG scheme is uniformly first-order convergent for general steady drift-diffusion-reaction equations, meaning that its error constant does not depend on the gradient of the solution, a result that was proved in [20] by a two-grid method and in [21] with a decomposition of the solution in the boundary layer. Gartland [22] proposed in further a family of uniformly convergent schemes of arbitrary order, the exponentially fitted HODIE schemes, which are compact and utilized auxiliary evaluation points within the compact stencil. For the literature of exponential fitted schemes, we refer to [21]. More recently, ten Thije Boonkkamp and Anthonissen introduced an improvement of the SG scheme that is derived from the solution of the stationary drift-diffusion equations including the source term. The resulting flux is a combination of two parts: a homogeneous component which is similar to the Scharfetter-Gummel flux in the case of constant coefficients, and an inhomogeneous part which integrates the source term. Liu et al. [23] later proved that this scheme is uniformly second-order convergent.

In particular for semiconductors, the use of SG scheme for charge continuity equations is somewhat favorable. During our bibliographical search for a *high-order* SG-typed scheme, we encountered numerous variations of the SG scheme. Without trying to be complete, we would like to cite some related works here. Markowich et al. [24] exerted that if the prescribed doping profile has an exponentially decaying internal layer, then so does the potential and the carrier densities, and the global error of the SG method depends only on the mesh size and the layer width. Furthermore, Chatard [25] proved that the SG scheme preserves the thermal equilibrium steady state. Bessemoulin-Chatard et al. [26] also demonstrated that the scheme is asymptotic preserving in the quasi-neutral limit by a compactness argument. Eymard et al. [27] extended the scheme for nonlinear diffusion and nonlinear advection, but their approach necessitates solving a nonlinear integral at each time step. Bessemoulin-Chatard [28] modified the scheme for nonlinear drift-diffusion equations with power-law pressure which does not require nonlinear solvers, and proved that the scheme also preserves the thermal equilibrium state if the densities are not vanishing. Patriarca et al. [29] later continued the approach of [27] and proposed solving the nonlinear integrals by

quadrature rules and Newton's method. Other than the SG scheme, other methods have been suggested and studied for the discretization of the continuity equations. Chainais-Hillairet et al. [30, 31, 32] used the first-order upwind scheme for the convective flux and the central scheme for the diffusive flux which proves to be convergent as the mesh is refined. Bessemoulin-Chatard and Filbet [33] modified the scheme by defining an enthalpy function (available in the case of power-law pressure) such that the convective and diffusive parts are discretized at the same time. The resulting scheme preserves the thermal equilibrium, even with vanishing densities.

Other than semiconductors, drift-diffusion equations are also present in hydrodynamic models of gas discharge. In the last decades experiments have shown that electric discharges could alter air flows hence an alternative technique for flow control. Numerical simulations have been conducted to study different plasma actuators, for instance the dielectric barrier discharge [34, 35] and wire-to-wire corona discharge [36] actuators. Other applications of atmospheric discharge are, for example, anti-icing [37]. In this article, we mainly take interest in the thermal equilibrium hydrodynamics model with mobility laws, which consists of drift-diffusion equations for every charged specie in the plasma, coupled with a Poisson equation for the electrostatic field ϕ,

$$\begin{aligned} \partial_t \rho_k - \nabla \cdot (D_k \rho_k + \rho_k z_k \mu_k \nabla \phi) &= S_k + S_{ph}, \\ -\varepsilon_0 \nabla \cdot \nabla \phi &= \sum_k \rho_k, \end{aligned}$$

where D_k, z_k, μ_k are resp. the diffusion rate, the charge number and the mobility of the specie k. The source term S_k represents chemical changes in the plasma, stemming from the inter-specie inelastic collisions (ionization, attachment, recombination, excitation, etc.), that affect the charge population of k. Finally the source term S_{ph} represents the photoionization effect.

As observed in [34] and in our own simulations, the SG scheme provides inadequate simulation results on insufficiently refined grids since it degenerates to first order in advection-dominant regimes. Therefore, high-order schemes such as the MUSCL method are used instead in [35, 38, 36, 39]. High-order methods allow simulations to be done on coarse grids (but sufficiently refined to capture the plasma dynamics) that save precious computation time. The preliminary question in this article is: *are there high-order schemes that are derived in the same manner as the SG scheme?* An interest of SG is that, as we know, it integrates at the same time the convective and diffusive parts. In our knowledge, so far there is no answers to this question. Some of the works that we cited on the semiconductors aimed to adapt the SG scheme to different particle statistics, hence the modified schemes are still first-order in drift-dominant cases. An exception is [40] where the proposed scheme is globally second-order. Another improved SG scheme is proposed by Kulikovsky [41] in which he assumed that the drift velocity is locally linear and used ghost points near the interface to evaluate the flux, therefore he added a first-order correction to the SG flux. Kulikovsky applied successfully his method to simulate the propagation of streamers in [42, 43].

In this article, we propose a framework to answer the preliminary question. The interests of our work are twofold: the new high-order schemes improve the accuracy of the numerical results, hence allow to decrease the computation charge; on the other

hand, the SG-based schemes discretize both the convective and diffusive fluxes, thus they set up a simple way to approximate the flux density. The structure of this article is set as follows: Section 2 describes the construction of the new family of high-order SG-based schemes, which are baptized *Scharfetter-Gummel schemes with Correction of Current* (SGCC); in Section 3 we study some of their numerical properties; academic tests are proposed in Section 4 to study the convergence order of SGCC compared to some other schemes; in Section 5 we describe more complex test cases in atmospheric gas discharge, e.g. a wire-to-wire corona discharge and a positive streamer propagation; the numerical results of these two simulations are presented in Section 6.

2. Design of the Scharfetter-Gummel schemes with Correction of Current

2.1. A brief recall of the Scharfetter-Gummel scheme

In 1969, Scharfetter and Gummel [1] proposed an approach to approximate the current density in (1). Assume that we have a mesh $0 = x_{1/2} < x_{3/2} < \cdots < x_{I-1/2} < x_{I+1/2} = 1$ with x_i $(1 \le i \le I)$ the center of $\Omega_i \overset{\Delta}{=} (x_{i-1/2}, x_{i+1/2})$, $\Delta x_i \overset{\Delta}{=} x_{i+1/2} - x_{i-1/2}$ and $\Delta x_{i+1/2} \overset{\Delta}{=} x_{i+1} - x_i$. The Scharfetter-Gummel (SG) method consists of solving, for each $0 \le i \le I$, the ordinary differential equation in x variable

$$-D_{i+1/2}\partial_x \rho(x) + u_{i+1/2}\rho(x) = j^{SG}_{i+1/2}, \quad x \in (x_j, x_{j+1}), \tag{4}$$

$$\rho(x_j) = \rho_j, \quad \rho(x_{j+1}) = \rho_{j+1}, \tag{5}$$

which is issued from (2) where u, D, j are supposed to be locally constant on $[x_j, x_{j+1}]$, resp. equal to $u_{i+1/2}$, $D_{i+1/2}$, $j^{SG}_{i+1/2}$. Solving (4)-(5), we obtain the *semi-discrete* flux

$$j^{SG}_{i+1/2} \overset{\Delta}{=} \frac{D_{i+1/2}}{\Delta x_{i+1/2}}\Big(\mathcal{B}(\alpha_{i+1/2})\rho_i - \mathcal{B}(-\alpha_{i+1/2})\rho_{i+1}\Big), \quad \text{for } 0 \le i \le I,$$

where

$$\alpha_{i+1/2} \overset{\Delta}{=} -\frac{u_{i+1/2}\Delta x_{i+1/2}}{D_{i+1/2}}, \quad \mathcal{B}(\alpha) \overset{\Delta}{=} \frac{\alpha}{e^\alpha - 1},$$

are resp. the numerical Péclet number and the Bernoulli function. The calculation of $j^{SG}_{1/2}$ and $j^{SG}_{I+1/2}$ requires the values of ρ_0 and ρ_{I+1} which are located outside of the computation domain. These values should be prescribed in accordance with boundary conditions.

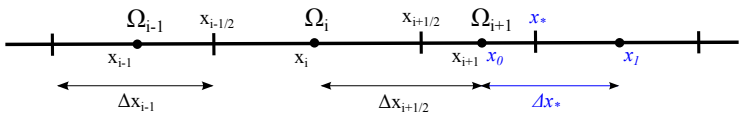

Figure 1: (colored) Spatial grid. In black: notations with global indices. In blue: notations with local indices.

In the finite-volume framework, the semi-discrete (with respect to the variable x) Scharfetter-Gummel scheme for (1)-(2) reads

$$\frac{\mathrm{d}\bar{\rho}_i(t)}{\mathrm{d}t} + \frac{\bar{j}^{SG}_{i+1/2} - \bar{j}^{SG}_{i-1/2}}{\Delta x_i} = 0, \quad 0 \le i \le I.$$

where $\bar{\rho}_i(t)$ is the average of $\rho(t,x)$ on the volume Ω_i,

$$\bar{\rho}_i(t) \triangleq \frac{1}{\Delta x_i}\int_{\Omega_i}\rho(t,x)\mathrm{d}x, \tag{6}$$

and the *numerical* flux

$$\bar{j}^{SG}_{i+1/2} \triangleq \frac{D_{i+1/2}}{\Delta x_{i+1/2}}\Big(\mathcal{B}(\alpha_{i+1/2})\bar{\rho}_i - \mathcal{B}(-\alpha_{i+1/2})\bar{\rho}_{i+1}\Big), \quad 0 \le i \le I.$$

2.2. A generalization of the Scharfetter-Gummel method

In this paper, we propose a generalization of the approach presented in the previous subsection. In (4), we consider instead a polynomial approximation $J_{i+1/2}(x)$ of the true flux j on the right-hand side. A p-order polynomial, centered at $x_{i+1/2}$ has the form $J_{i+1/2}(x) = J^{(0)} + J^{(1)}(x - x_{i+1/2}) + \cdots + \frac{1}{p!}J^{(p)}(x - x_{i+1/2})^p$ with $J^{(q)} \in \mathbb{R}$, $0 \le q \le p$. Note that the numerical flux equals to the evaluation of $J_{i+1/2}$ at $x_{i+1/2}$, thus equals to $J^{(0)}$. The other $J^{(q)}$ are introduced to correct $J^{(0)}$ as we shall see. The local ODE that was introduced in the previous subsection now becomes

$$-D_{i+1/2}\partial_x\rho(x) + u_{i+1/2}\rho(x) = J_{i+1/2}(x), \quad x \in (x_i, x_{i+1}) \tag{7}$$

For the sake of simplicity, in the following when there is no ambiguity, we replace the subscripts $_i$, $_{i+1/2}$ and $_{i+1}$ by resp. $_0$, $_*$ and $_1$ (see Figure 1). Now deriving (7) q times ($0 \le q \le p$) yields

$$-D_*\partial_x^{q+1}\rho(x) + u_*\partial_x^q\rho(x) = \sum_{m=q}^{p}\frac{1}{(m-q)!}J^{(m)}(x - x_*)^{m-q}, \quad x \in (x_0, x_1). \tag{8}$$

We define the notations $\partial_x^q\rho_b \triangleq \partial_x^q\rho(x_b)$ ($b = 0, 1$). For each q we solve the ODE (8) on (x_0, x_1) and by some algebraic manipulations we have

$$J^{(q)} = \frac{D_*}{\Delta x_*}\Big(\mathcal{B}(\alpha_*)\partial_x^q\rho_0 - \mathcal{B}(-\alpha_*)\partial_x^q\rho_1\Big) - \sum_{m=q+1}^{p}\frac{1}{(m-q)!}J^{(m)}(\Delta x_*)^{m-q}\psi_*^{(m-q)}, \tag{9}$$

where

$$\psi_*^{(m)} = \frac{\int_{-\chi}^{\kappa}\xi^m\mathrm{e}^{\alpha_*\xi}d\xi}{\int_{-\chi}^{\kappa}\mathrm{e}^{\alpha_*\xi}d\xi} = \mathrm{e}^{\alpha_*\chi}\mathcal{B}(\alpha_*)\int_{-\chi}^{\kappa}\xi^m\mathrm{e}^{\alpha_*\xi}d\xi, \tag{10}$$

$$\text{or else} \quad \psi_*^{(m)} \triangleq \frac{\kappa^m\mathrm{e}^{\alpha*} - (-\chi)^m}{\mathrm{e}^{\alpha_*} - 1} - \frac{m}{\alpha_*}\psi_*^{(m-1)} \quad \text{with } \psi_*^{(0)} = 1, \tag{11}$$

$$\alpha_* \triangleq -\frac{u_*\Delta x_*}{D_*}, \quad \kappa \triangleq \frac{\Delta x_1}{2\Delta x_*}, \quad \chi \triangleq \frac{\Delta x_0}{2\Delta x_*}.$$

With $p + 1$ equations of the form (9), a general expression of the flux $J^{(0)}$ can be worked out by recursion. Before a such result is achievable, the equations in (9) should be written in a more compact form in order to be serviceable to the formulation of $J^{(0)}$. This point is addressed by the subsequent lemma which is easily demonstrated by induction.

Lemma 1. *$J^{(q)}$ can be written in an alternative expression*

$$J^{(q)} = \frac{D_*}{\Delta x_*}\Big(\mathcal{B}(\alpha_*)Q_0^{(q)} - \mathcal{B}(-\alpha_*)Q_1^{(q)}\Big),$$

where $Q_b^{(q)}$ ($b = 0, 1$) satisfy the following recurrence relation

$$Q_b^{(p)} = \partial_x^p \rho_b, \tag{12}$$

$$Q_b^{(q)} = \partial_x^q \rho_b - \sum_{m=q+1}^{p} \frac{(\Delta x_*)^{m-q}\psi_*^{(m-q)}}{(m-q)!} Q_b^{(m)}, \quad 0 \le q < p. \tag{13}$$

Furthermore, as $Q_b^{(q)}$ depend only on the $Q_b^{(k)}$'s with $k > q$, and by virtue of (12)-(13)*, they depend only on the spatial derivatives of ρ*

$$Q_b^{(q)} = \sum_{k=q}^{p} \Theta(k, q)\partial_x^k \rho_b, \quad 0 \le q \le p, \tag{14}$$

where the auxiliary terms $\Theta(k, q)$ ($k \ge q$) satisfy: For $q \le p$,

$$\Theta(q, q) = 1, \tag{15}$$

$$\Theta(k, q) = -\sum_{m=q+1}^{k} \frac{(\Delta x_*)^{m-q}\psi_*^{(m-q)}}{(m-q)!}\Theta(k, m), \quad k > q, \tag{16}$$

$$\Theta(k, q) = \Theta(p, p-k+q), \quad q \le k \le p. \tag{17}$$

The final point of Lemma 1 asserts that only $\Theta(p, p-q), q \le p$ need to be computed. For that cause the following lemma is useful.

Lemma 2. *Let $I_m(q)$ denote the set of strictly positive m-tuples $(x_1, x_2, \ldots, x_m)$ whose sum of elements equals q*

$$I_m(q) \stackrel{\Delta}{=} \Big\{\boldsymbol{X} = (x_1, x_2, \ldots, x_m) \text{ such that } x_n \in \mathbb{N}^* \quad \forall 1 \le n \le m, \quad x_1 + \cdots + x_m = q\Big\}.$$

Then

$$\Theta(p, p) = 1, \tag{18}$$

$$\Theta(p, p-q) = (\Delta x_*)^q \sum_{k=1}^{q} (-1)^k \sum_{\boldsymbol{X} \in I_k(q)} \prod_{x_n \in \boldsymbol{X}} \left(\frac{\psi_*^{(x_n)}}{x_n!}\right), \quad 1 \le q < p. \tag{19}$$

Proof. (18) is trivial (from Lemma 1). For $q = 1, 2$, from (16)

$$\Theta(p, p-1) = -\sum_{m=p}^{p} \frac{(\Delta x_*)^{m-p+1}\psi_*^{(m-p+1)}}{(m-p+1)!}\Theta(p, m) = -\Delta x_* \psi_*^{(1)}$$

$$\Theta(p, p-2) = -\sum_{m=p-1}^{p} \frac{(\Delta x_*)^{m-p+2}\psi_*^{(m-p+2)}}{(m-p+2)!}\Theta(p, m) = -\Delta x_* \psi_*^{(1)}\Theta(p, p-1) - \frac{(\Delta x_*)^2\psi_*^{(2)}}{2}$$

$$= (\Delta x_*)^2(-1)^2\psi_*^{(1)}\psi_*^{(1)} + (\Delta x_*)^2(-1)\frac{\psi_*^{(2)}}{2}.$$

Therefore (19) is true for $q = 1, 2$. Suppose that it is also true for $0, 1, \ldots, q-1$, then from (16)

$$\begin{aligned}\Theta(p, p-q) &= -\sum_{m=p-q+1}^{p} \frac{(\Delta x_*)^{m-p+q}\psi_*^{(m-p+q)}}{(m-p+q)!}\Theta(p,m) = -\sum_{m=0}^{q-1} \frac{(\Delta x_*)^{q-m}\psi_*^{(q-m)}}{(q-m)!}\Theta(p,p-m) \\ &= -\sum_{m=1}^{q-1} \frac{(\Delta x_*)^{q-m}\psi_*^{(q-m)}}{(q-m)!}(\Delta x_*)^m \sum_{k=1}^{m}(-1)^k \sum_{\boldsymbol{X}\in I_k(m)} \prod_{x_n\in\boldsymbol{X}} \left(\frac{\psi_*^{(x_n)}}{x_n!}\right) - \frac{(\Delta x_*)^q\psi_*^{(q)}}{q!} \\ &= (\Delta x_*)^q \sum_{k=1}^{q-1}(-1)^{k+1} \frac{\psi_*^{(q-m)}}{(q-m)!} \sum_{m=k}^{q-1} \sum_{\boldsymbol{X}\in I_k(m)} \prod_{x_n\in\boldsymbol{X}} \left(\frac{\psi_*^{(x_n)}}{x_n!}\right) - \frac{(\Delta x_*)^q\psi_*^{(q)}}{q!}.\end{aligned} \tag{20}$$

Now we remark that there are two equivalent manners to find all the tuples $\boldsymbol{Y} \in I_{k+1}(q)$.

1. *Direct method.* All strictly positive $(k+1)$-tuples $\boldsymbol{Y} = (x_1, x_2, \ldots, x_k, x_{k+1})$ such that $x_1 + \cdots + x_{k+1} = q$, are directly listed.
2. *Recurrent method.* Start by finding all strictly positive k-tuples $\boldsymbol{X} = (x_1, x_2, \ldots, x_k)$ such that $x_1 + \cdots + x_k = m$, $k \le m \le q-1$. Then complete $\boldsymbol{Y}$ by appending $x_{k+1} = q - m$ to the end of $\boldsymbol{X}$. The lower bound of m is due to $x_1, \ldots, x_k \ge 1$ thus $x_1 + \cdots + x_k \ge k$, the upper bound is due to $x_{k+1} \ge 1$.

The equivalence of the two tuple-finding methods yields

$$\sum_{\boldsymbol{Y}\in I_{k+1}(q)} \prod_{x_n\in\boldsymbol{Y}} \left(\frac{\psi_*^{(x_n)}}{x_n!}\right) = \sum_{m=k}^{q-1} \frac{\psi_*^{(q-m)}}{(q-m)!} \sum_{\boldsymbol{X}\in I_k(m)} \prod_{x_n\in\boldsymbol{X}} \left(\frac{\psi_*^{(x_n)}}{x_n!}\right).$$

Thus from (20),

$$\begin{aligned}\Theta(p, p-q) &= (\Delta x_*)^q \sum_{k=1}^{q-1}(-1)^{k+1} \sum_{\boldsymbol{Y}\in I_{k+1}(q)} \prod_{x_n\in\boldsymbol{Y}} \left(\frac{\psi_*^{(x_n)}}{x_n!}\right) - \frac{(\Delta x_*)^q\psi_*^{(q)}}{q!} \\ &= (\Delta x_*)^q \sum_{k=2}^{q}(-1)^{k} \sum_{\boldsymbol{X}\in I_k(q)} \prod_{x_n\in\boldsymbol{X}} \left(\frac{\psi_*^{(x_n)}}{x_n!}\right) + (\Delta x_*)^q(-1) \sum_{\boldsymbol{X}\in I_1(q)} \prod_{x_n\in\boldsymbol{X}} \left(\frac{\psi_*^{(x_n)}}{x_n!}\right) \\ &= (\Delta x_*)^q \sum_{k=1}^{q}(-1)^{k} \sum_{\boldsymbol{X}\in I_k(q)} \prod_{x_n\in\boldsymbol{X}} \left(\frac{\psi_*^{(x_n)}}{x_n!}\right).\end{aligned}$$

Finally the number of terms in (19) can always be checked in prior with the equality $Card(I_k(q)) = \binom{q-1}{k-1}$. □

Ultimately, an expression of the semi-discrete flux $j_{i+1/2}^{\mathrm{SGCC}_p} \triangleq \boldsymbol{J}^{(0)}$, in function of the derivatives of ρ, is drawn from (14)-(18)-(19). The scheme name SGCC is an abbreviation of ***S**charfetter-**G**ummel scheme with **C**orrection of **C**urrent*, the subscript $_p$ stands for the reconstruction polynomial order of the flux. The result of this subsection is summarized in Definition 1.

Definition 1. *The semi-discrete flux of the SGCC$_p$ scheme reads*

$$j_{i+1/2}^{SGCC_p} \triangleq \frac{D_{i+1/2}}{\Delta x_{i+1/2}}\Big(\mathcal{B}\left(\alpha_{i+1/2}\right) Q_i^{(0)} - \mathcal{B}\left(-\alpha_{i+1/2}\right) Q_{i+1}^{(0)}\Big),$$

where

$$Q_i^{(0)} = \rho_i + \sum_{q=1}^{p} (\Delta x_{i+1/2})^q W_{i+1/2}^{(q)} \partial_x^q \rho_i, \quad W_{i+1/2}^{(q)} \triangleq \frac{\Theta_{i+1/2}(p, p-q)}{(\Delta x_{i+1/2})^q} = \sum_{k=1}^{q} (-1)^k \sum_{\boldsymbol{X} \in I_k(q)} \prod_{x_n \in \boldsymbol{X}} \left(\frac{\psi_{i+1/2}^{(x_n)}}{x_n!} \right),$$

with the ψ functions defined in (10)*/*(11)*.*

2.3. The limiting cases $\alpha = \infty$ and $\alpha = 0$

It is instructive to inquire the limits of the flux $j_*^{\mathrm{SGCC}_p}$ when $\alpha \to \infty$ and $\alpha \to 0$. On a uniform mesh, it is well known that the classical Scharfetter-Gummel scheme automatically switches between the second-order central scheme when the diffusion is dominant ($\alpha << 1$, recall that $\alpha = -u_* \Delta x_* / D_*$), and the first-order upwind scheme in advection-dominant regime ($\alpha >> 1$). Since the SGCC$_p$ flux is constructed in the same principle, it is natural to think that it inherits this automatic switching property.

Let us cite at first a useful lemma which is straightforward from (10)-(11)-(20).

Lemma 3. *The Bernoulli function, the $\psi_*^{(q)}$ functions and the $W_*^{(q)}$ are smooth with respect to α. Furthermore the $\psi_*^{(q)}$ functions and the $W_*^{(q)}$ functions are bounded. We have, for $q \geq 1$,*

$$\lim_{\alpha \to 0} \mathcal{B}(\alpha) = 1, \quad \lim_{\alpha \to +\infty} \mathcal{B}(\alpha) = 0, \quad \mathcal{B}(\alpha) \sim -\alpha \quad (\alpha \to -\infty),$$

$$\lim_{\alpha \to 0} \psi_*^{(q)}(\alpha) = \frac{\kappa^{q+1} - (-\chi)^{q+1}}{q+1}, \quad \lim_{\alpha \to +\infty} \psi_*^{(q)}(\alpha) = \kappa^q, \quad \lim_{\alpha \to -\infty} \psi_*^{(q)}(\alpha) = (-\chi)^q,$$

$$\lim_{\alpha \to +\infty} W_*^{(q)}(\alpha) = \frac{(-\kappa)^q}{q!}, \quad \lim_{\alpha \to -\infty} W_*^{(q)}(\alpha) = \frac{\chi^q}{q!},$$

$$\sum_{q=0}^{k} \frac{\kappa^{k-q+1} - (-\chi)^{k-q+1}}{(k-q+1)!} U_*^{(q)} = 0 \quad (k \leq 1),$$

with

$$\kappa \triangleq \frac{\Delta x_1}{2\Delta x_*}, \quad \chi \triangleq \frac{\Delta x_0}{2\Delta x_*}, \quad U_*^{(q)} \triangleq \lim_{\alpha \to 0} W_*^{(q)}(\alpha).$$

Proof. The equalities on the two first lines are straightforward from the definition of the Bernoulli function and from (10)-(11). The equalities on the last two lines are obtained by induction using the second equality in (20). □

With the tools in Lemma 3, we can derive the limits of SGCC$_p$.

Proposition 1. *In the convective limit $\alpha \to -\infty$, we have*

$$\lim_{\alpha\to-\infty} j_*^{SGCC_p} = \rho_0 + \sum_{q=1}^{p} \frac{1}{q!}\left(\frac{\Delta x_0}{2}\right)^q \partial_x^q \rho_0.$$

If $\alpha \to +\infty$ bears the opposite sign, then

$$\lim_{\alpha\to+\infty} j_*^{SGCC_p} = \rho_1 + \sum_{q=1}^{p} \frac{1}{q!}\left(-\frac{\Delta x_1}{2}\right)^q \partial_x^q \rho_1.$$

On the contrary, in the diffusive limit $\alpha \to 0$, and assuming that ρ is sufficiently smooth on (x_0, x_1), then

$$\lim_{\alpha\to0} j_*^{SGCC_p} = D_*\partial_x\rho_* + O(h^{p+1}), \quad \textit{with } h \triangleq \max \Delta x_i.$$

Proof. Using Lemma 3 and Taylor's expansion of ρ at x_* up to the $(p+1)^{th}$ derivative, we have

$$\begin{aligned}
\lim_{\alpha\to0} j_*^{\mathrm{SGCC}_p} &= \frac{D_*}{\Delta x_*}\sum_{q=0}^{p} (\Delta x_*)^q U_*^{(q)}\left(\partial_x^q\rho_1 - \partial_x^q\rho_0\right) \\
&= \frac{D_*}{\Delta x_*}\sum_{q=0}^{p} (\Delta x_*)^q U_*^{(q)} \sum_{k=1}^{p-q+1} \frac{1}{k!}(\Delta x_*)^k \partial_x^{q+k}\rho_*\left(\kappa^k - (-\chi)^k\right) + O(h^{p+1}) \\
&= \frac{D_*}{\Delta x_*}\sum_{k=0}^{p} (\Delta x_*)^{k+1}\partial_x^{k+1}\rho_* \sum_{q=0}^{k} \frac{\kappa^{k-q+1} - (-\chi)^{k-q+1}}{(k-q+1)!} U_*^{(q)} + O(h^{p+1}) \\
&= D_*\partial_x\rho_* + O(h^{p+1}),
\end{aligned}$$

with $U_*^{(0)} = 1$ and the fact that $\kappa + \chi = 1$. □

From this point of view, the semi-discrete SGCC_p flux reduces to the semi-discrete high-order upwind flux using a p-order polynomial reconstruction of ρ when the advection is dominant. On the other hand when the diffusion is dominant, the SGCC_p flux behaves as a $(p+1)$-order approximation of the gradient of ρ (scaled the diffusion rate D_*) at the interface x_*.

2.4. The finite volume $SGCC_p$ scheme

In the finite volume framework, we use the cell averages $\bar{\rho}_i$ (6) instead of the exact values $\rho_i \triangleq \rho(x_i)$. In the flux equation (1), the slopes $\partial_x^q\rho_i \triangleq \partial_x^q\rho(x_i)$ $(1 \le q \le p)$ are replaced by their discrete counterparts $\Delta^{(q)}\bar{\rho}_i$ which are reconstructed from the $\bar{\rho}_i$'s (see for example [15]), whereas the quantity ρ_i is substituted by a discrete one denoted $\Delta^{(0)}\bar{\rho}_i$. If we introduce the polynomial reconstruction of ρ on the cell Ω_i as

$$\tilde{\rho}_i(x) \triangleq \Delta^{(0)}\bar{\rho}_i + \sum_{q=1}^{p} \frac{1}{q!}\Delta^{(q)}\bar{\rho}_i (x - x_i)^q, \quad x \in \Omega_i,$$

then the value of $\Delta^{(0)}\bar{\rho}_i$ stems from the local density conservation,

$$\frac{1}{\Delta x_i}\int_{\Omega_i}\tilde{\rho}_i(x)\mathrm{d}x = \frac{1}{\Delta x_i}\int_{\Omega_i}\rho(x)\mathrm{d}x \triangleq \bar{\rho}_i.$$

Thus

$$\Delta^{(0)}\bar{\rho}_i = \bar{\rho}_i - \sum_{q=1}^{p}\Delta^{(q)}\bar{\rho}_i z_i^{(q)} \quad \text{with} \quad z_i^{(q)} \triangleq \frac{1}{\Delta x_i}\int_{\Omega_i}\frac{1}{q!}(x-x_i)^q\mathrm{d}x.$$

Finally, the finite volume SGCC$_p$ reads

$$\frac{\mathrm{d}\bar{\rho}_i(t)}{\mathrm{d}t} + \frac{\bar{j}^{\mathrm{SGCC}_p}_{i+1/2} - \bar{j}^{\mathrm{SGCC}_p}_{i-1/2}}{\Delta x_i} = 0, \quad 0 \le i \le I,$$

with

$$\bar{j}^{\mathrm{SGCC}_p}_{i+1/2} \triangleq \frac{D_{i+1/2}}{\Delta x_{i+1/2}}\Big(\mathcal{B}\left(\alpha_{i+1/2}\right)\bar{Q}_i^{(0)} - \mathcal{B}\left(-\alpha_{i+1/2}\right)\bar{Q}_{i+1}^{(0)}\Big),$$

$$\bar{Q}_i^{(0)} = \Delta^{(0)}\bar{\rho}_i + \sum_{q=1}^{p}(\Delta x_{i+1/2})^q W_{i+1/2}^{(q)}\Delta^{(q)}\bar{\rho}_i.$$

Remark 1. *The stencil of the SGCC$_p$ flux is the same as classical MUSCL approach with high-order reconstruction. Its complexity is augmented due to exponential terms such as $\mathcal{B}(\alpha)$ and $W^{(q)}$. Therefore computation time is slightly longer (see Section 6.2, Table 5).*

3. Numerical analysis

For simplicity, we assume that u and D are constant throughout this section.

3.1. Flux consistency of the SGCC$_p$ schemes

Lemma 4. *Let f be a regular function, $f \in C^{p+1}(x_0, x_1)$, satisfying*

$$\int_{x_0}^{x_1}\partial_x^q f(x)g(x)\mathrm{d}x = 0, \quad q \le p, \tag{21}$$

with g a positive integrable function on (x_0, x_1). Then there exists a constant $C > 0$ independent of $\Delta x_* \triangleq x_1 - x_0$ such that for all $x \in (x_0, x_1)$,

$$|f(x)| \le C(\Delta x_*)^{p+1}.$$

Proof. Using Taylor's theorem and the smoothness of f, for each $0 \le q \le p$ and $x \in (x_0, x_1)$ we have

$$\partial_x^q f(x) = \sum_{m=q}^{p}\frac{\partial_x^m f(x_*)}{(m-q)!}(x-x_*)^{m-q} + R_p^q(x), \tag{22}$$

with the rest

$$R_p^q(x) \triangleq \int_{x_*}^{x} \frac{\partial_x^{p+1} f(t)}{(p-q)!}(x-t)^{p-q}\mathrm{d}t$$

thus, assuming that $x > x_*$ without loss of generality,

$$\left|R_p^q(x)\right| \leq M \int_{x_*}^{x} \frac{(x-t)^{p-q}}{(p-q)!}\mathrm{d}t \leq \frac{M}{(p-q+1)!}\left(\frac{\Delta x_*}{2}\right)^{p-q+1}, \quad \text{with } M \triangleq \sup_{t\in(x_0,x_1)}\left(\left|\partial_x^{p+1} f(t)\right|\right).$$

Then from (21), (22) and the positivity of g we have, for $0 \leq q \leq p-1$,

$$\left|\partial_x^q f(x_*)\right| \leq \sum_{m=q+1}^{p} \frac{\left|\partial_x^m f(x_*)\right|}{(m-q)!}\left(\frac{\Delta x_*}{2}\right)^{m-q} + \frac{M}{(p-q+1)!}\left(\frac{\Delta x_*}{2}\right)^{p-q+1},$$

and $\left|\partial_x^p f(x_*)\right| \leq M\Delta x_*/2$. We verify easily that $\left|\partial_x^{p-1} f(x_*)\right| \leq 3M/2(\Delta x_*/2)^2$. Therefore by prescribing that $\left|\partial_x^m f(x_*)\right| < Mc_m(\Delta x_*/2)^{p+1-m}$ for all m greater than a certain q and c_m are constants (for example $c_p = 1$), and let $c_{p+1} = 1$ we have

$$\left|\partial_x^q f(x_*)\right| \leq M\left(\frac{\Delta x_*}{2}\right)^{p-q+1} \sum_{m=q+1}^{p+1} \frac{c_m}{(m-q)!}.$$

It is straightforward to see that $\{c_m\}_{m=0,\ldots,p+1}$ is a decreasing series and $1 + 1/2! + \cdots + 1/k! < \mathrm{e} - 1$ for all natural number k. These yield

$$\left|\partial_x^q f(x_*)\right| \leq M(\mathrm{e}-1)c_{q+1}\left(\frac{\Delta x_*}{2}\right)^{p-q+1}.$$

Thus we assume that $c_q = (\mathrm{e}-1)c_{q+1}$ and by induction we have $c_q = (\mathrm{e}-1)^{p-q}c_p = (\mathrm{e}-1)^{p-q}$. Finally for all $q \leq p$ we have

$$\left|\partial_x^q f(x_*)\right| \leq M(\mathrm{e}-1)^{p-q}\left(\frac{\Delta x_*}{2}\right)^{p-q+1}$$

Therefore, from (22), for all $x \in (x_0, x_1)$,

$$\left|\partial_x^q f(x)\right| \leq M\left(\frac{\Delta x_*}{2}\right)^{p-q+1}\left(\sum_{m=q}^{p}\frac{(\mathrm{e}-1)^{p-m}}{(m-q)!} + \frac{1}{(p-q+1)!}\right) < M(\mathrm{e}-1)^{p-q+1}\left(\frac{\Delta x_*}{2}\right)^{p-q+1}.$$

In particular for $q = p$ we have $|f(x)| \leq C(\Delta x_*)^{p+1}$ with $C = M(\mathrm{e}-1)^{p+1}/2^{p+1}$. □

Let us now underline a property that is inherited by the p^{th}-order reconstruction polynomial $J_{i+1/2}$ through its construction process. In (8) it is required that $\partial_x^q J_{i+1/2} = -D\mathrm{e}^{-\varphi}(\mathrm{e}^{\varphi}\partial_x^q\rho)'$ on (x_i, x_{i+1}), with $\varphi' = -u/D$. Passing the variables that are not under derivation to the left-hand side and integrating over (x_i, x_{i+1}) yields

$$\int_{x_0}^{x_1} \partial_x^q J_{i+1/2}(x)\frac{\mathrm{e}^{\varphi(x)}}{D}\mathrm{d}x = \left[\mathrm{e}^{\varphi}\partial_x^q\rho\right]_{x_1}^{x_0}.$$

This equation is also satisfied by the derivatives of the true flux j, therefore Lemma 4 is applicable with $f = j - J_{i+1/2}$ and $g = \mathrm{e}^{\phi}$. As $j_{i+1/2}^{\mathrm{SGCC}_p} = J_{i+1/2}(x_{i+1/2})$, the following proposition is straightforward.

Proposition 2. *The $SGCC_p$ scheme is consistent in the sense that*

$$\left| j_{i+1/2}^{SGCC_p} - j(x_{i+1/2}) \right| < Ch^{p+1}, \quad \textit{for all } 1 \le i \le I,$$

where $h \triangleq \max_i \Delta x_i$, $C = M(\mathrm{e}-1)^{p+1}/2^{p+1}$, $M = \sup_{t\in(x_i,x_{i+1})} \left(\left| \partial_x^{p+1} j(t) \right| \right)$.

3.2. L^∞-stability and TVD property of the $SGCC_1$-TVD schemes

In Section 2.4, we remarked that discrete approximates of the gradients are required to construct the discrete flux. In this section, we investigate some properties of the SGCC_1 flux combined with the TVD slopes [9, 44, 8]. The resulting schemes are named SGCC_1-TVD.

Let us present a (very brief) sketch of the TVD slope limiters. The space step Δx and the time step Δt are assumed to be **constant** in the following. Without loss of generality, consider that $u > 0$. On the cell Ω_i the solution is reconstructed with a slope

$$\sigma_i^n = \frac{\overline{\rho}_{i+1}^n - \overline{\rho}_i^n}{\Delta x} \Phi(\theta_i^n) \quad \text{with} \quad \theta_i^n = \frac{\overline{\rho}_i^n - \overline{\rho}_{i-1}^n}{\overline{\rho}_{i+1}^n - \overline{\rho}_i^n}.$$

The so-called slope-limiter function Φ is introduced to damp any possible over/under-shootings of the reconstruction. But not every choice of Φ could suppress oscillations, for instance $\Phi \equiv 1$ (Lax-Wendroff scheme). For this to work, the slope limiter is required to lie in Sweby's region [8],

$$\begin{gathered} \Phi = 0 \quad \text{for} \quad \theta < 0, \\ \theta \le \Phi \le 2\theta \quad \cap \quad \Phi \le 1 \quad \text{for} \quad 0 \le \theta < 1, \\ \Phi \le \theta \quad \cap \quad 1 \le \Phi \le 2 \quad \text{for} \quad \theta \ge 1. \end{gathered} \tag{23}$$

These requirements are met so that the schemes are second-order in space (for smooth solutions) and TVD. The latter one is a consequence of Harten's theorem [9]. Let us cite an extension of this theorem.

Theorem 1. *Suppose that a numerical scheme is written in the form*

$$\rho_i^{n+1} = \rho_i^n + a_i^n(\rho_{i+1}^n - \rho_i^n) - b_{i-1}^n(\rho_i^n - \rho_{i-1}^n). \tag{24}$$

Then if $a_i^n \ge 0$, $b_i^n \ge 0$ and

- *if $a_i^n + b_i^n \le 1$, the scheme is TVD,*
- *if $a_i^n + b_{i-1}^n \le 1$, the scheme is L^∞-stable.*

In case of our SGCC$_1$-TVD scheme, the TVD slope σ_i^n (23) is used in place of $\Delta^{(1)}\bar{\rho}_i^n$. The numerical scheme is written in the form (24) with

$$a_i^n = B\left(1 + W^{(1)}\frac{\Phi_{i+1}^n}{\theta_{i+1}^n}\right), \quad b_{i-1}^n = A\left(1 - W^{(1)}\Phi_{i-1}^n\right) + (A+B)W^{(1)}\frac{\Phi_i^n}{\theta_i^n},$$

$$A = \frac{\Delta t}{(\Delta x)^2}D\mathcal{B}(\alpha), \quad B = \frac{\Delta t}{(\Delta x)^2}D\mathcal{B}(-\alpha),$$

$$\alpha = -\frac{u\Delta x}{D}, \quad W^{(1)} = -\frac{1}{2}\frac{\mathrm{e}^\alpha + 1}{\mathrm{e}^\alpha - 1} + \frac{1}{\alpha} = -\frac{1}{2}\coth\left(\frac{\alpha}{2}\right) + \frac{1}{\alpha}.$$

Proposition 3. *In the light of Theorem 1, the SGCC$_1$-TVD scheme are TVD and L^∞-stable if the following CFL-like condition is fulfilled,*

$$\Delta t \leq \frac{\Delta x}{2u}\tanh\left(\frac{u\Delta x}{2D}\right).$$

Proof.

1. Let us first notice that $A, B > 0$ and $0 \leq W^{(1)} \leq 1/2$ since $\alpha < 0$. With Φ_i^n satisfying (23), it is straightforward that $a_i^n \geq 0$ and $b_{i-1}^n \geq 0$.
2. The inequality $a_i^n + b_i^n \leq 1$ is equivalent to

$$1 - \frac{A}{A+B}W^{(1)}\Phi_i^n + \frac{A+2B}{A+B}W^{(1)}\frac{\Phi_{i+1}^n}{\theta_{i+1}^n} \leq \frac{1}{A+B}.$$

But we have

$$0 \leq \frac{A}{A+B}W^{(1)}\Phi_i^n \leq 1, \quad 0 \leq \frac{A+2B}{A+B}W^{(1)}\frac{\Phi_{i+1}^n}{\theta_{i+1}^n} \leq 2\frac{A+2B}{A+B}W^{(1)},$$

It can be shown that $\frac{A+2B}{A+B}W^{(1)}$ is decreasing and bounded by $1/2$ and 0 for $\alpha < 0$, so

$$\left|\frac{A}{A+B}W^{(1)}\Phi_i^n - \frac{A+2B}{A+B}W^{(1)}\frac{\Phi_{i+1}^n}{\theta_{i+1}^n}\right| \leq 1,$$

then

$$1 - \frac{A}{A+B}W^{(1)}\Phi_i^n + \frac{A+2B}{A+B}W^{(1)}\frac{\Phi_{i+1}^n}{\theta_{i+1}^n} \leq 2.$$

Thus the scheme is TVD if $A + B \leq 1/2$ which is equivalent to the stated CFL condition since $\mathcal{B}(\alpha) + \mathcal{B}(-\alpha) = \alpha\coth(\alpha/2)$.

3. The L^∞-stability of the scheme is proven in the same way since $a_i^n + b_{i-1}^n \leq 1$ is equivalent to

$$1 - \frac{A}{A+B}W^{(1)}\Phi_{i-1}^n + \frac{B}{A+B}W^{(1)}\frac{\Phi_{i+1}^n}{\theta_{i+1}^n} + W^{(1)}\frac{\Phi_i^n}{\theta_i^n} \leq \frac{1}{A+B},$$

and

$$0 \leq \frac{A}{A+B}W^{(1)}\Phi_{i-1}^n \leq 1, \quad 0 \leq \frac{B}{A+B}W^{(1)}\frac{\Phi_{i+1}^n}{\theta_{i+1}^n} + W^{(1)}\frac{\Phi_i^n}{\theta_i^n} \leq 2\frac{A+2B}{A+B}W^{(1)} \leq 1.$$

□

Remark 2. *In the case of variable u, D, let u_i^n, D_i^n denote the values of u, D at time level t^n on cell center x_i. In practical implementation we use the following estimation for the advancing time step Δt^n,*

$$\Delta t^n = c \min_i \left\{ \frac{\Delta x_i}{u_i^n} \tanh\left(\frac{u_i^n \Delta x_i}{2D_i^n} \right) \right\}, \tag{25}$$

where $c \in (0, 1/2]$ is an adjustable parameter.

4. Convergence tests

We begin numerical test with two one-dimensional examples to test the spatial accuracy of the new SGCC_1 and SGCC_2 schemes. The *superbee* limiter is incorporated in the former one while the generalized moment limiter [16] (GML) is used in the latter. Throughout this part, we consider uniform meshes and the third-order SSP-Runge-Kutta scheme [45] is used for time discretization. The CFL condition satisfies (25) with $c = 0.4$. The first example is the ideal transport-diffusion of a Gaussian hat with a constant diffusion rate and drift velocity. The other taken from [41] is the transport-diffusion of a hyperbolic tangent profile.

Example 1 (moving Gaussian hat). We consider $(0, T) \times \Omega = (0, 0.25) \times (0, 1)$, a drift velocity $u = 1$ and a diffusion rate D taking three different values: 10^{-2}, 10^{-4} and 10^{-6}. The boundary conditions are homogeneous Neumann. The initial profile is

$$\rho_0(x) = \exp\left(-\frac{(x - x_0)^2}{2\sigma} \right),$$

with $x_0 = 0.25$ and $\sigma = 10^{-4}$. Since the profile is numerically zero and flat near the edges and the diffusion is weak, we consider that the exact solution is

$$\rho_{ex}(t, x) = \left(\frac{\sigma}{2Dt + \sigma} \right)^{\frac{1}{2}} \exp\left(-\frac{(x - x_0 - ut)^2}{4Dt + 2\sigma} \right).$$

For a grid of size Δx, the total discretization error in L_1-norm is defined as $e_{\Delta x} \overset{\Delta}{=} \|\rho_{\Delta x}(T) - \rho_{ex}(T)\|_{L_1(\Omega)}$. An estimation of the convergence order is then given by $\log_2(e_{\Delta x}/e_{\Delta x/2})$. The numerical results are grouped in Tables 1-2-3. We can observe that when the diffusion is large ($D = 10^{-2}$), the classical SG, SGCC_1, MUSCL schemes are second-order. Meanwhile the SGCC_2 scheme is fourth-order, which is predictable from the Taylor's expansion in the proof of Proposition 1 for the diffusive limit. Indeed, as the grid is uniform, the coefficient of the $(p+1)^{th}$ derivative would vanish if p is even. The convergence orders deteriorate with the diffusion rate. The SG scheme is at most first-order since the convection is dominant. On the contrary the SGCC_1 and MUSCL schemes maintain more or less a high convergence order. Overall SGCC_1 displays more accuracy than MUSCL. It is worth noted that the embedded TVD limiters are first-order at extrema, so while the grid is sparse it is comprehensible that these schemes are first-order. The same argument can be applied for the SGCC_2 scheme which, by the GML

method, uses sequentially the *minmod* limiter on the reconstructed slopes. But overall, the SGCC_2 scheme is third-order in convection-dominant regimes.

I	SG		SGCC_1		SGCC_2		MUSCL	
	L_1-error	order	L_1-error	order	L_1-error	order	L_1-error	order
100	3.26×10^{-2}	_	1.62×10^{-2}	_	1.71×10^{-2}	_	1.63×10^{-2}	_
200	2.79×10^{-2}	0.23	4.96×10^{-3}	1.72	6.85×10^{-3}	1.32	4.95×10^{-3}	1.72
400	2.22×10^{-2}	0.33	3×10^{-3}	0.72	1.92×10^{-3}	1.84	3×10^{-3}	0.72
800	1.64×10^{-2}	0.43	1.35×10^{-3}	1.15	2.88×10^{-4}	2.73	1.35×10^{-3}	1.15
1600	1.11×10^{-2}	0.56	6.98×10^{-4}	0.96	3.59×10^{-5}	3.00	7.01×10^{-4}	0.95
3200	6.9×10^{-3}	0.69	2.49×10^{-4}	1.49	4.55×10^{-6}	2.98	2.51×10^{-4}	1.49

Table 1: *Example 1,* $D = 10^{-6}$. Convergence order in L_1-norm. Errors in function of number of grid cells I.

I	SG		SGCC_1		SGCC_2		MUSCL	
	L_1-error	order	L_1-error	order	L_1-error	order	L_1-error	order
100	2.95×10^{-2}	_	1.24×10^{-2}	_	1.34×10^{-2}	_	1.25×10^{-2}	_
200	2.43×10^{-2}	0.28	2.99×10^{-3}	2.05	4.4×10^{-3}	1.6	3.06×10^{-3}	2.03
400	1.82×10^{-2}	0.42	1.7×10^{-3}	0.82	9.35×10^{-4}	2.23	1.77×10^{-3}	0.79
800	1.2×10^{-2}	0.6	8.36×10^{-4}	1.02	1.21×10^{-4}	2.95	1.01×10^{-3}	0.81
1600	6.49×10^{-3}	0.89	2.03×10^{-4}	2.04	1.38×10^{-5}	3.13	3.22×10^{-4}	1.64
3200	2.56×10^{-3}	1.34	4.28×10^{-5}	2.24	1.33×10^{-6}	3.38	8.83×10^{-5}	1.86

Table 2: *Example 1,* $D = 10^{-4}$. Convergence order in L_1-norm.

I	SG		SGCC_1		SGCC_2		MUSCL	
	L_1-error	order	L_1-error	order	L_1-error	order	L_1-error	order
100	9.73×10^{-4}	_	2.25×10^{-4}	_	1.7×10^{-5}	_	4.89×10^{-4}	_
200	2.54×10^{-4}	1.94	5.63×10^{-5}	2	1.04×10^{-6}	4.03	1.71×10^{-4}	1.52
400	6.42×10^{-5}	1.98	1.4×10^{-5}	2.01	6.31×10^{-8}	4.04	4.58×10^{-5}	1.9
800	1.61×10^{-5}	2	3.49×10^{-6}	2	3.9×10^{-9}	4.02	1.16×10^{-5}	1.98
1600	4.02×10^{-6}	2	8.71×10^{-7}	2	2.43×10^{-10}	4	2.93×10^{-6}	1.99
3200	1.01×10^{-6}	2	2.78×10^{-7}	2	1.56×10^{-11}	3.96	7.33×10^{-7}	2

Table 3: *Example 1,* $D = 10^{-2}$. Convergence order in L_1-norm.

Example 2 (moving canyon). We take $(0, T) \times \Omega = (0, 4 \times 10^{-5}) \times (0, 1)$, $u = -Ax$, $D = 1$ and

$$\rho_0(x) = n_1 + \frac{n_2}{2}\left(1 + \tanh\left(\frac{x - x_0}{\sigma}\right)\right),$$

with $A = 10^4$, $n_1 = 10^2$, $n_2 = 10^{12}$, $x_0 = 0.7$ and $\sigma = 0.02$. If we neglect the diffusion term, the solution to the resulting convection equation, which could serve as a benchmark, is

$$\rho(t, x) = \rho_0 \left(x e^{At} \right) e^{At}.$$

In Figure 2 we illustrate the numerical solutions at final time T of the SG-based schemes on a grid of 200 equal cells. Solutions of MUSCL are utterly close to $SGCC_1$ so they are not displayed. Two choices of TVD limiters are embedded in $SGCC_1$. The *superbee* limiter produced a stairy solution since it is very compressing. On the other hand, the *minmod* limiter is more relaxing, thus it generated a smooth solution. The SG scheme is too diffusive as its slide is far more chubby than the others. Finally, the $SGCC_2$ scheme also gave a wavy but smoother solution since we used a generalized minmod limiter to limit the slopes. Overall, this solution is the closest to the benchmark.

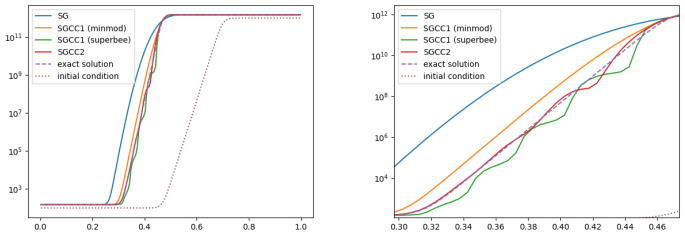

(a) Panorama. (b) Zoom.

Figure 2: (colored) *Example 2.* Numerical and pseudo-exact solutions at $T = 4 \times 10^{-5}$ of different schemes with $I = 200$. y-axis in log scale.

5. Gas discharge simulations

In this sections, the robustness and the reliability of our new schemes $SGCC_1$ and $SGCC_2$ in simulations of atmospheric gas discharge are tested. Two configurations are considered here: a wire-to-wire corona discharge on the time scale of milliseconds and a positive streamer propagation between two planar electrodes that happens in nanoseconds. Simulations with the SG and MUSCL schemes are also presented to compare the accuracy.

5.1. Plasma discharge in one dimension: a corona discharge

A corona discharge is a type of glow discharge in air that occurs in presence of a highly non-uniform electric field. In this subsection, we study the effect of our new SG-based schemes on a wire-to-wire corona discharge. The configuration is proposed in [36]: the corona actuator consists of two cylindrical wires put parallel and separated by a distance $d = 40mm$. The radii of the anode and the cathode are resp. $r_1 = 0.35mm$

and $r_2 = 1mm$. A tension $V_G = 40kV$ is applied between two wires, see Figure 3. An analytical formula of the resulting electrostatic potential ϕ_L,

$$\nabla \cdot \nabla \phi_L = 0,$$
$$\phi(\text{anode}) = V_G, \quad \phi(\text{cathode}) = 0,$$

is given in [36]. In the same paper, a quasi-2D numerical model was proposed in [36] in which the plasma is assumed to extend over a dome-like zone of thickness $S(x)$ between the electrodes. Instead of working in (x, y) plane, we now solve the equations on the axis that bridges the wire centers ($y = 0$), with the volume element $dv = S(x)dx$.

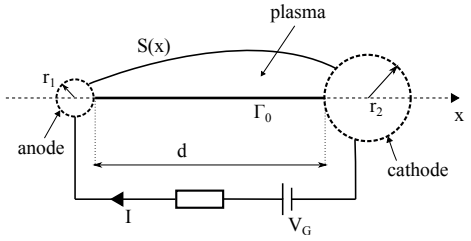

Figure 3: Sketch of a wire-to-wire configuration.

In this numerical model, the photoionization is not considered. Neither is the ion diffusion, since their temperature is the same as air hence thermal fluctuation is negligible. On the other hand, electrons are supposed to be at thermal equilibrium, meaning that their internal energy depends only on the field, hence so do the transport, diffusion and reaction coefficients. By affecting a change of variable with $q \triangleq S\rho$, the quasi-2D corona reads as follows,

$$\begin{aligned}
\partial_t q_e - \mu_e E q_e + D_e \frac{\partial_x S}{S} q_e - D_e \partial_x q_e &= \omega_e, \\
\partial_t q_+ + \mu_+ E q_+ &= \omega_+, \\
\partial_t q_- - \mu_- E q_- &= \omega_-, \\
-\varepsilon_0 \partial_x (S \, \partial_x \phi_c) &= q_e + q_+ + q_-,
\end{aligned}$$

$$E = -\partial_x(\phi_L + \phi_c), \tag{26}$$

with ϕ_c the electric potential in the presence of the plasma space charge between the electrodes (therefore $\phi_c(\text{anode}) = \phi_c(\text{cathode}) = 0$) and the source terms given by

$$\omega_e = (\alpha - \eta) q_e - \frac{k_{e,+}}{eS} q_e q_+, \quad \omega_+ = -\alpha q_e + \frac{k_{e,+}}{eS} q_e q_+ + \frac{k_{+,-}}{eS} q_+ q_-, \quad \omega_- = \eta q_e - \frac{k_{+,-}}{eS} q_+ q_-,$$

where $\alpha, \eta \, (s^{-1})$ are resp. the ionization and attachment frequencies, e is the elementary charge ($\approx 1.602 \times 10{-}19C$), $k_{e,+}$, $k_{+,-}$ $(m^{-3}s^{-1})$ are resp. the electron-ion and ion-ion recombination coefficients. In our simulations, $\mu_+ = \mu_- = 3.5 \times 10^{-4} m^2 V^{-1} s^{-1}$,

$k_{e,+} = k_{+,-} = 2 \times 10^{-13} m^{-3} s^{-1}$. The coefficients α and η are calculated using the BOLSIG+ code [46] and tabulated.

The computation domain is the line denoted Γ_0 in Figure 3. This line is discretized into cells such that the left interface of the first cell and the right interface of the last cells coincide resp. with the anode and cathode surfaces. A mesh refinement technique is employed to capture the intense dynamics near the electrodes and relax the grid size in the calmer inter-electrode region: at first we construct a uniform grid, we compute the plasma thickness S at grid centers, then we construct a new grid with the same number of cells where its size is proportional to S.

Since photoionization is not considered, a homogeneous background charge ρ_b is maintained for all species. In the follow-up simulations we take $\rho_b = \pm e \times 10^9 Cm^{-3}$ with the sign depending on charge sign. This is also the initial conditions used in the simulations.

Dirichlet boundary conditions are used for all species: $\rho_k(\text{anode}) = \rho_k(\text{cathode}) = \rho_b$ with $k = e, +, -$. An additional source of electrons comes from the cathode where the arriving ions bombard the wire surface resulting in a secondary emission of electrons. This emission is characterized by a coefficient γ that depends on various parameters such as the electrode material, the surface roughness, the gas composition, etc. In this work we take $\gamma = 10^{-4}$. The secondary emission changes the electronic current density as follows

$$j_e(\text{cathode}) = -\gamma j_+(\text{cathode}), \quad \text{with } j_e = -\mu_e E q_e + D_e \frac{\partial_x S}{S} q_e - D_e \partial_x q_e, \quad j_+ = \mu_+ E q_+.$$

The total current density (in $Cm^{-2}s^{-1}$) is the sum of the conductive and displacement current density [36],

$$j_t \stackrel{\Delta}{=} j_e + j_+ + j_- + \varepsilon_0 \partial_t E.$$

Without trying to be complete, the current I in the external circuit can be computed using an approach proposed by Sato [47]. The following formula for I is taken directly from [36], with a minor change since the anode electric potential is unchanged in our simulations: $I = L \int_{\Gamma_0} j_t \partial_x f \mathrm{d}v$, where L is the length of the wires. In our simulations, $L = 16cm$.

Since ions weigh much heavier than electrons, their drifting time is also much longer. As we use explicit time integration, the CFL condition on each specie is very unequal. Furthermore, as we shall see, the electric field in this type of discharge is not affected tremendously by the space charge, hence the field relaxation characteristic time is also not restrictive. Therefore a sub-cycling strategy [35] is employed to boost the simulation time: the transport of ions and the electric field are frozen on a large time step while computing the electron transport and the chemical reactions for which the time steps is tremendously smaller due to the intense dynamics of electrons. Strang's operator splitting is used for solve separately the transport and the chemical reactions. The second-order SSP-Runge-Kutta/Heun's method is used for time integration. The CFL condition satisfies (25) with $c = 0.49$. The P_1-Lagrange finite element method is used to solve the field equation (26). The classical upwind MUSCL scheme is used to

applied to the ion transport equations. Finally, the MUSCL, SG, $SGCC_1$ and $SGCC_2$ are employed to solve the electron drift-diffusion equation.

Overall the numerical model is second-order, but the idea is to compare the influence of different schemes on the electrons. We employ the notation ^{I}SG (for example) to imply a result obtained by the scheme SG on the (locally refined) I-cell grid.

5.2. Plasma discharge in two dimensions: a streamer propagation

The second test of gas discharge in atmospheric pressure is taken directly from [48]. This is a simulation of a positive streamer propagation. We refer to [49, 50] on the physics of this type of discharge. The numerical model considered here only takes into account the electron and positive ion densities and the transport of ions is neglected providing the short time scale of streamer propagation, reads as follows,

$$\begin{aligned}
\partial_t \rho_e - \mu \mathbf{E} \cdot \nabla \rho_e - D \nabla \cdot \nabla \rho_e &= (\alpha - \eta)\mu |\mathbf{E}| \rho_e, \\
\partial_t \rho_i &= -(\alpha - \eta)\mu |\mathbf{E}| \rho_e, \\
-\varepsilon_0 \nabla \cdot \nabla \phi &= \rho_i + \rho_e, \\
\mathbf{E} &= -\nabla \phi.
\end{aligned}$$

In dry air, containing $80\%N_2$ and $20\%O_2$ at pressure $P = 750Torr$ and room temperature $T = 273K$, the electron mobility μ, the electron diffusion rate D, the ionization coefficient α and the reattachment coefficient η are given analytically [48] as

$$\mu = 2.3987|\mathbf{E}|^{-0.26} \quad (m^2 V^{-1} s^{-1}), \quad D = 4.3628 \times 10^{-3} |\mathbf{E}|^{0.22} \quad (m^2 s^{-1}), \quad \eta = 340.75 \quad (m^{-1}), \tag{27}$$

$$\alpha = (1.1944 \times 10^6 + 4.3666 \times 10^{26} / |\mathbf{E}|^3) \mathrm{e}^{2.73 \times 10^7 / |\mathbf{E}|} \quad (m^{-1}). \tag{28}$$

The set of equations are numerically solved in the axisymmetric coordinates (r, z). The streamer propagates along a gap between a planar cathode placed at $z = 0$ and an anode placed at $z_{\max} = 1.25cm$. On the radial side the domain stretches between $r = 0$ and $r_{\max} = 1.25cm$. A potential $\phi_0 = 18.75kV$ is applied at the anode, giving rise to an axial and homogeneous electric field of $E_L = -15kVcm^{-1}$ which is well below the breakdown field. Homogeneous Neumann boundary condition is applied for the potential at $r = r_{max}$ and for the electron density at all boundaries except $r = 0$. To initiate the formation of a streamer, a Gaussian seed of positive ions is injected into the domain (see Figure 4),

$$\rho_+(t = 0, r, z) = \rho_0 \exp\left(-\frac{r^2 + (z - z_0)^2}{\sigma^2}\right),$$

with $\rho_0 = e \times 5 \times 10^{18} Cm^{-3}$ (e is the elementary charge), $\sigma = 0.4mm$ and $z_0 = 1cm$. In these streamer simulations, we do not consider the electrons source by photoionization. To compensate the creation of charges through this process, homogeneous background density levels of $\rho_b = \pm e \times 10^{13} Cm^{-3}$ for the first test case and $\rho_b = \pm e \times 10^9 Cm^{-3}$ for the second case are used, both for the electrons and the ions. Finally, the simulations stop at $T = 16ns$.

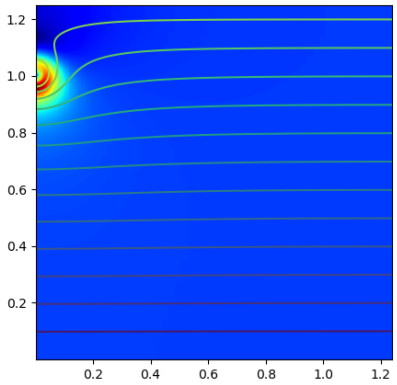

Figure 4: (colored) Initial electric field generated by a Gaussian ions cloud centered at $z = 1cm$ and equipotential lines. The planar anode is situated at the upper border at $z = 1.25cm$, the cathode lies at the lower border at $z = 0$. The left border at $r = 0$ is the symmetry axis, meanwhile homogeneous Neumann condition is applied for the potential at the right border at $r = 1.25cm$.

Mesh-wise, rectangular cells are used throughout the simulations so that directional splitting is straightforward. We use the Strang splitting [51] to maintain high accuracy. The third order SSP-Runge-Kutta method [45] is used for time discretization. The CFL condition satisfies (25) with $c = 0.4$. In the z-direction, the space step is constant and the number of cells are a power of 2, so that the Poisson's equation on the potential is tensorized by applying Fourier's transform in z. In r, the one dimensional elliptic equation corresponding to each frequency is numerically solved with a finite volume scheme. Finally, the finite volume method is employed to discretize the electrons transport equation. Several schemes are used to construct the numerical fluxes, namely the SG scheme, the MUSCL scheme, the SGCC_1 scheme and the SGCC_2 scheme. The *superbee* limiter is used in the MUSCL and SGCC_1 schemes; meanwhile the generalized moment limiter [16] is used in the SGCC_2 scheme.

Numerical results are presented in Subsection 6.2 to compare the influence of different numerical schemes on the electrons transport. For each scheme, three simulations are carried out with decreasing mesh sizes. The first mesh consists of 262 cells on the r direction and 4096 cells on the z direction. Since the space step on the z direction is constant, we have $\Delta z \approx 3\mu m$. On the r direction, similar space step $\Delta r_{\min} \approx \Delta z$ is imposed from $r = 0$ to $r = 600\mu m$ and space steps are gradually larger beyond. Similar discretization strategy is used for other meshes. The second mesh consists of 400 cells on the r direction and 8192 cells on the z direction, $\Delta r_{\min} \approx \Delta z \approx 1.5\mu m$. The third mesh has 600×16384 cells, $\Delta r_{\min} \approx \Delta z \approx 0.8\mu m$. We employ the notation SG^a (for example) to imply a result obtained by the scheme SG on the mesh of minimal space step a.

6. Simulation results

6.1. Simulation 1: plasma discharge in one dimension - a corona discharge

At $t = 0$, a potential $V_G = 40kV$ is applied on the anode, abruptly causing breakdowns around the electrodes. In Figure 5 we display the evolution of the field strength and specie densities within the first $210\mu s$ of the discharge, obtained by $^{400}\mathrm{SGCC}_2$. The anode lies at $x = 0$ and the cathode at $x = 40mm$. At $t = 0$ the field strength at the anode over $10MVm^{-1}$ and at the cathode is $4MVm^{-1}$ which surpasses the critical ignition value $3.75MVm^{-1}$, thus we expect ionization at both electrodes but mainly at the anode. Within the first $10\mu s$, multiple highly energized avalanches occur ahead the latter, producing a high-density cloud of ions with $n_+ = n_- = 2 \times 10^{17}m^{-3}$ (Figure 5c, d). Meanwhile, the electrons are all absorbed by the anode. The field drops critically because of the screening effect. This process thus affects the current intensity in the external circuit. Indeed, at $t = 1\mu s$ we observe a current surge of about $200\mu A$ (Figure 6a) due to steep variation of the field and electron absorption. At $t = 10\mu s$ that the current drops significantly to about $25\mu A$ since the displacement and electron conducting currents vanish. After $t = 10\mu s$ we enter the ion collection phase where the ions drift towards the opposite-sign electrode. As the positive cloud departs the screening effect around the anode fades away and the field strength gradually increases. From $t = 60\mu s$ on, the field is only slightly distorted in the middle region due to ion drifting and ionization stably takes place at the anode, forming a positive corona. The newly creating positive ions follow closely the previous departing ions cloud to the cathode (Figure 5c) where a sink separates the two populations that slightly decreases the current at $t = 250\mu s$ (Figure 6a). On the other hand, since the ionization is no longer disrupted, the anode is perpetually surrounded by an electron cloud that becomes more and more populated (Figure 5b), thus increases the external current. The weak ionization and secondary emission also form a permanent electron cloud just ahead the cathode. A cloud of negative ions appears at the beginning due to high concentration of electrons and attachment, then drifting towards the anode while attachment still occurs and increases the ion level in front of the ion wave (Figure 5d). From about $t = 500\mu s$ the ion levels in the middle region are quasi constant and continue to increase until reaching a steady state.

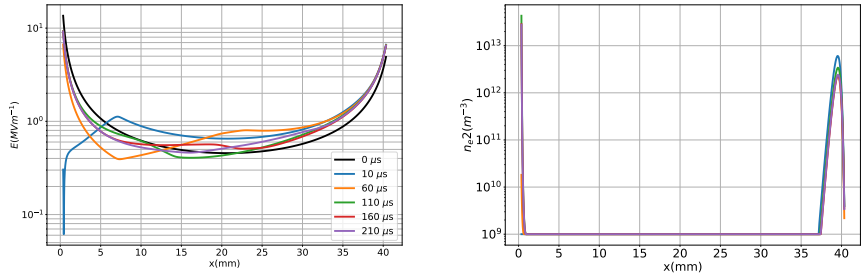

(a) Field strength $|E|$ (MVm^{-1}).

(b) Electron density $n_e = -\rho_e/e$ (m^{-3}).

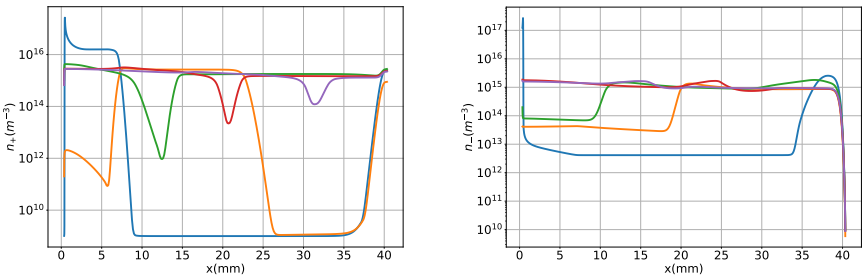

(c) Positive ion density $n_+ = \rho_+/e$ (m^{-3}).

(d) Negative ion density $n_- = -\rho_-/e$ (m^{-3}).

Figure 5: (colored) *Simulation 1.* Evolution of field strength and specie densities. Results of $^{400}\text{SGCC}_2$.

In Figure 6 we compare the currents obtained by four schemes: MUSCL, SG, SGCC_1 and SGCC_2. We mainly present the results on 400 and 800-cell grids, since the computation time on more refined grids is absurd. Therefore, we only present the result of ^{3200}MUSCL up to $T = 290\mu s$ as reference. In Figure 6a we compare the currents on long time scale ($T = 4ms$) where a steady state is reached. We observe a tendency that the current decreases as the mesh is refined. Accordingly, the SG scheme overestimates the current intensity comparing to the reference curve (in black) and the standard MUSCL scheme. Even ^{800}SG gives a less accurate result than ^{400}MUSCL. The SGCC_1 scheme is close to MUSCL, meaning that they have roughly the same accuracy. Interestingly, SGCC_2 gives visually the same current on both grids which also agrees with the reference curve before $T = 290\mu s$, thus the scheme is highly accurate. Figure 6b displays a zoom from $110\mu s$ to $290\mu s$ on the currents. Although MUSCL and SGCC_1 provide fair results, on the 400-cell grid the maximal discrepancy is $10\mu A$, roughly 15% of the reference current. $^{400}\text{SGCC}_2$ is on the other hand exceptionally close to ^{3200}MUSCL, even better than ^{800}MUSCL and $^{800}\text{SGCC}_1$.

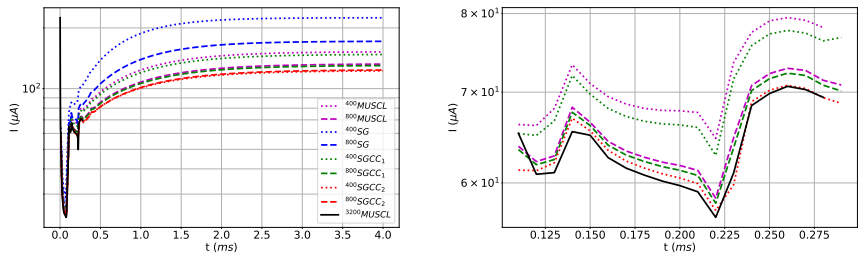

(a) $t = 0 - 4ms$ (b) $t = 0.11 - 0.29ms$

Figure 6: (colored) *Simulation 1.* Comparison of external current I with different schemes and grids, on long time (left) and short time (right).

6.2. Plasma discharge in two dimensions - a streamer propagation

6.2.1. Simulation 2: high background density

In this section, the streamer propagation is simulated with a pre-ionized electrons and ions background of $\rho_b = \pm e \times 10^{13} Cm^{-3}$. The four considered numerical schemes are SG, MUSCL, SGCC_1 and SGCC_2 with different meshes described in Section 5.2. In Figure 7, aerial view of the evolution of the field strength $|\mathbf{E}|$, computed with the $\text{SGCC}_2^{3.0}$ scheme, is illustrated. We can clearly observe that the Gaussian seed enhances the electric field and transforms into a positive streamer within about $4ns$ that propagates in the direction of the cathode with a round leading front of high field intensity. The field strength in this narrow region can exceed $14MVm^{-1}$ which is well beyond the breakdown field $2.5MVm^{-1}$ (when α (28) begins to take over η (27)). It is the ionization avalanches that take place in this thin layer that play a decisive role of the streamer advancement [50]. On the way to the cathode, the streamer leaves behind a dark-colored weak field trace. This is the quasi-neutral region consisting of almost equal amount of free electrons and ions that forms a plasma conducting channel [50]. Figure 8b shows a cross view of the axial field E_z in dotted lines and the total space charge $\rho_{tot} = \rho_+ + \rho_e$ in solid lines on the axis $r = 0$. Again a gradient layer of E_z can be observed in advancement along with a small but highly concentrated positive space charge front. In a cathode-directed streamer, this positive front acts as a beacon attracting pre-ionized electrons from outside the conducting channel. The arriving electrons ionize the gas in front of the gradient layer, then move inwards the channel, neutralizing the existing gradient layer but leaving behind newborn ions. Since the pre-ionized electrons are produced by energized photons emitted by the beacon [50], it is absolutely crucial to apply a background charge density in the absence of the photo-ionization source term as in the previous corona discharge simulations. In Figure 8a, the evolution of electron density $n_e = -\rho_e/e$ is given. Within $4ns$, the density increases exponentially until it reaches $1.4 \times 10^{20} m^{-3}$. This phase corresponds to the streamer formation. Beyond $4ns$, the electron level maintains between $1 - 1.2 \times 10^{20} m^{-3}$ in the quasi-neutral zone, this is the stable advancement phase of the streamer.

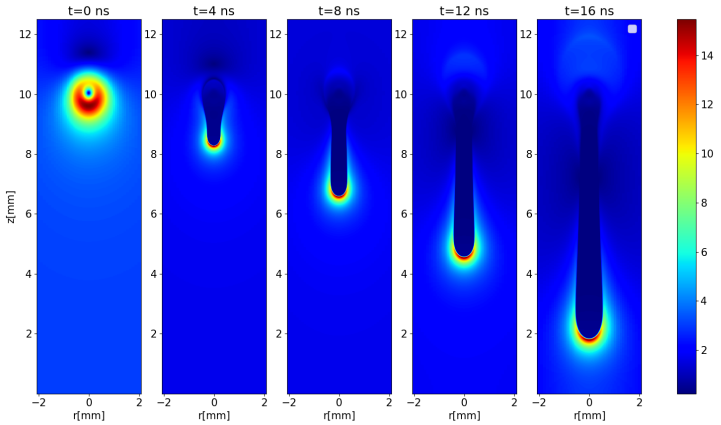

Figure 7: (colored) *Simulation 2.* Evolution of the electric field strength $|\mathbf{E}|$ (MVm^{-1}) of a downward propagation of the streamer. Results are obtained by $\mathrm{SGCC}_2^{3.0}$. Although the domain stretches to $r = 1.25cm$, visualization is only shown up to $r = 2mm$.

It is interesting to note that when the propagation is stable, the peak space charge $\rho_{\max}$ diminishes in time albeit the layer width R_ρ increases. R_ρ is measured as the distance between two point z_1, z_2 where $\rho_{tot}(z_1) = \rho_{tot}(z_2) = 1\%\rho_{\max}$. Moreover, the maximal field strength $E_{\max}$ in the layer is almost independent of time. This indicates that charge concentration in the layer should be more or less conserved in time. In a paper of Kulikovsky [42], a such property was put forth and verified by simulations with almost identical conditions as here. Kulikovsky postulated that from a electrostatic point of view, the electrical field at the layer is equivalent to that at the surface of a ball of radius R_ρ filled with uniformly distributed charge $\rho_{\max}$. Under this assumption he deduced a relation between the peak field strength and front charge,

$$E_{\max} \approx -\frac{\rho_{\max} R_\rho}{3\varepsilon_0} - E_L. \tag{29}$$

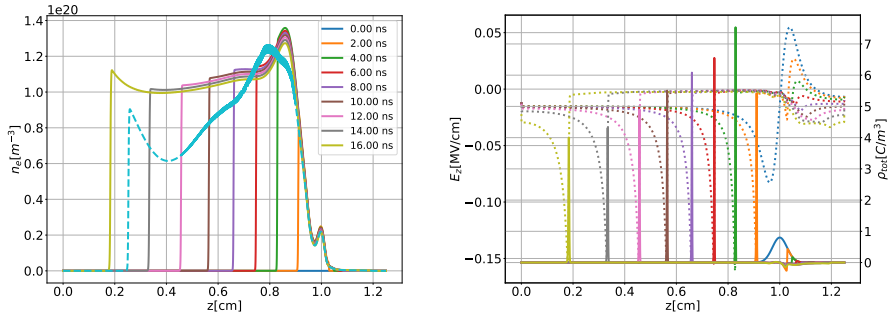

(a) Electrons density $n_e = -\rho_e/e$ (m^{-3}). The dashed line is the density at $16ns$ obtained by $\text{SGCC}_1^{3.0}$.

(b) Axial field E_z (MVm^{-1}) (dotted lines, left axis) and total space charge (Cm^{-3}) (solid lines, right axis).

Figure 8: (colored) *Simulation 2.* Evolution of the axial field and the space charge (right) and the electrons density (left) on the axis $r = 0$. Results obtained by $\text{SGCC}_2^{3.0}$.

In Table 4 we listed the aforementioned variables with values taken from our simulations with the $\text{SGCC}_1^{1.5}$, $\text{SGCC}_2^{3.0}$ and $\text{SGCC}_2^{1.5}$ schemes. We do not list those of the $\text{SGCC}_1^{3.0}$ scheme since oscillations of charge density are observed in this simulation (see Figure 8a) which make it difficult to extract the values of R_ρ. Same phenomenon is observed with the $\text{MUSCL}^{3.0}$ scheme. Since the simulation did carry on until the end, we suspect that the nature of these oscillations is not linked to the numerical schemes but to the coarse grid that failed to capture correctly the streamer dynamics. The results show that $\rho_{\max} R_\rho$ and $E_{\max}$ are effectively quasi-constant, albeit there is a 20% discrepancy regarding to (29).

	$4ns$	$8ns$	$12ns$	$16ns$
R_ρ (μm)	63/61/61	75/73/72	95/89/93	122/116/124
$\rho_{\max}$ (Cm^{-3})	7.7/7.5/8.2	6.2/6.1/6.5	4.8/4.9/4.9	3.9/4.0/4.0
$R_\rho \times \rho_{\max}/3/\varepsilon_0$ $(kVcm^{-1})$	181/173/187	174/169/174	172/163/172	179/175/184
$E_{\max}$ $(kVcm^{-1})$	163/161/167	156/154/158	151/150/153	156/155/159

Table 4: *Simulation 2.* Evolution of the charge front width R_ρ, the maximal front charge density $\rho_{\max}$ and the maximal field strength $E_{\max}$. Results obtained by $\text{SGCC}_1^{1.5}$/$\text{SGCC}_2^{3.0}$/$\text{SGCC}_2^{1.5}$.

So far we have shown the capability of the new SGCC_1 and SGCC_2 schemes in reproducing streamer propagation. The numerical results show consistency with the theory and other streamer simulations [48, 42, 52, 42, 43, 49]. Front charge conservation is also observed in accordance to [42]. We now compare the SG-based schemes with other existing schemes. Figure 9 show resp. the amplified streamer length in time and the peak field strength versus streamer length. The streamer length is defined as $L(t) = 1.25cm - z_{\max}(t)$, where $z_{\max}(t)$ is the location on the axis $r = 0$ where the electric field strength is maximal at time t. The streamer length is subtracted by vt with $v = 0.05$ to amplify the difference between the curves. The peak field strength

$E_{\max}$ at time t is measured at $z_{\max}(t)$ and $r = 0$. Four numerical schemes are considered: SG (blue), $SGCC_1$ (green), $SGCC_2$ (red), MUSCL (magenta) with three meshes: 262×4096 (square), 400×8192 (triangle), 600×16384 (cross). Table 5 show simulation time and computer model used for each test case. Existing simulation results extracted from [48] from two groups: **CWI** [39] and **FR** [38] are added as references. The CWI group used the 5-point central difference scheme to solve Poisson's equation, whereas the FR group used the Fourier-finite-volume method similar to us. Both group used the MUSCL scheme to discretize the electron continuity equation, albeit the CWI used Koren's limiter and the FR used the *superbee* limiter for stability. The results from these two groups are obtained on a grid with $\Delta r_{\min} \approx \Delta z \approx 0.8\mu m$.

Δz, $\Delta r_{\min}$	SG	$SGCC_1$	$SGCC_2$	MUSCL	Computer
$3\mu m$	2.1H	2.9H	3.3H	2.7H	Intel(R) Core(TM) i5-10210U CPU @ 1.60GHz
$1.5\mu m$	40H	44H	111H	41H	Intel(R) Core(TM) i5-10210U CPU @ 1.60GHz
$0.8\mu m$	187H	334H	768H	327H	Intel(R) Xeon(R) CPU E5-4650 0 @ 2.70GHz

Table 5: *Simulation 2.* Simulation times in hours. By default the simulations stop at $T = 16ns$; exceptions are $SG^{3.0}$ (13ns), $SG^{1.5}$ (15ns).

At first glance we can remark that the SG scheme gave total inadequate estimations. It overestimated both the streamer length and the peak field strength. Since the streamer enhances too fast, it reaches the cathode within only $13 - 15ns$, comparing to $16ns$ in simulations with other schemes. Even on the finest mesh, the blue curves deviate from the references with the largest marge 30% and 50% of the references. Similar overestimating behavior of the SG scheme was also observed in [52]. This is a huge drawback of the first-order SG method. The MUSCL and $SGCC_1$ schemes in the other hand provided much more trustworthy results. On the coarsest mesh, the largest discrepancy is both 20% of the references, while on the finest mesh it is only 10% and 2%. $SGCC_1$ however show slightly more deviation than MUSCL on the coarse grid, a fairly disappointing news. Since the streamer propagation is a (very) time-dependent problem, the advantage of $SGCC_1$ over MUSCL is somewhat blurred. It is noted that on the grid $3\mu m$, both MUSCL and $SGCC_1$ produced peak field strength that is not constant: there is a sink at $L = 0.9cm$; we also mentioned that the results of both schemes are polluted with small oscillations. Therefore, it is recommended to use better-resolution grid to obtain high-quality results. In general, both second-order schemes displayed good accuracy and mesh convergence. Finally, the $SGCC_2$ scheme show firmest results among the four methods. On the coarsest grid the red curves are already close to the references; in terms of peak field strength it highlights the front charge conservation in the streamer stable state, whilst others do not. It is also noted that the reference curves seem to not cluster at the same place as other curves on the finest grid (except for SG). In summary, in this test case all four numerical schemes display robustness and mesh convergence; among them the $SGCC_2$ scheme, being itself third-order, display highest accuracy. The results also show that the new SG-based schemes are capable of reproducing correctly and accurately a streamer propagation, a highly dynamic phenomenon of gas discharge.

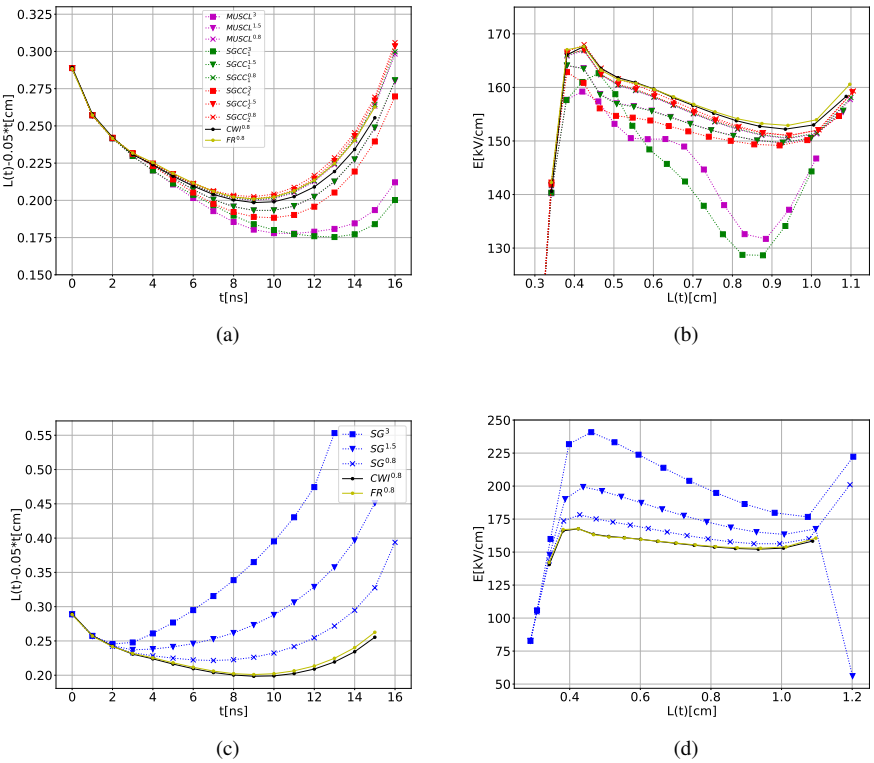

Figure 9: (colored) *Simulation 2.* Comparison of different numerical schemes: amplified streamer length $L - vt$ (cm) versus time with $v = 0.05cm.s^{-1}$ (left) and peak field strength $E_{\max}$ $(kVcm^{-1})$ versus streamer length (right). Note that at $\Delta r_{\min} = 1.5\mu m$ the results of MUSCL and SGCC_1 begin to superimpose. Reference curves in black and yellow.

6.2.2. Simulation 3: low background density

For these simulations, we use a background charge density of $\rho_b = \pm e \times 10^9 Cm^{-3}$. Similar grids and numerical schemes are used. The final time is $T = 23ns$. In Figure 10b, we observe that the level of electron density is almost as twice as in Simulation 2. Comparing to Simulation 2, Simulation 3 is more challenging due to steeper streamer front and the streamer takes longer time to complete the gap. With $\Delta z = 3\mu m$ only SGCC_2 succeeds to reach the end of simulation. SG crashes at $3ns$ and SGCC_1, MUSCL both crash at $10ns$ (see Figure 11c,d) due to the appearance of unstable oscillations. In Figure 10, we remark that these oscillations even persist for SGCC_1 (and MUSCL but not illustrated) with grid size $\Delta z = 1.5\mu m$, by the fact that the electron density forms a series of peaks along the streamer body and the field strength is laterally distorted. On the same grid, the results of SGCC_2 are smooth. On coarse grid, SGCC_2^3 behaves like $\text{SGCC}_1^{1.5}$ (not illustrated here) and manages to stay stable.

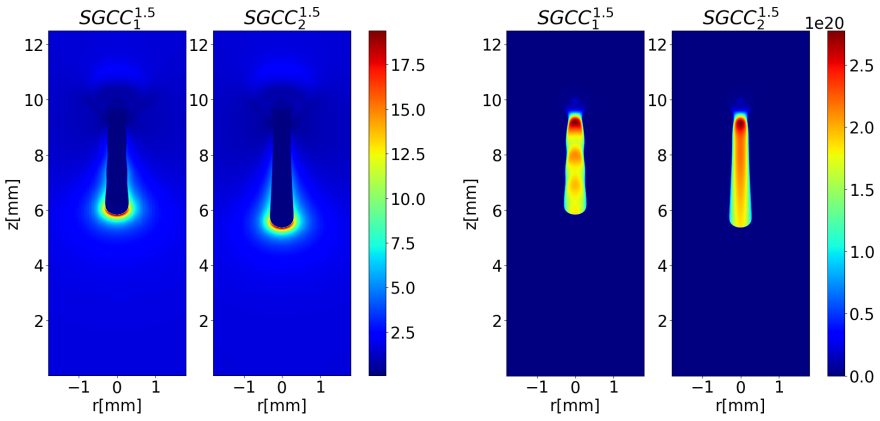

(a) Field strength $|\mathbf{E}|$ (MVm^{-1}).

(b) Electron density $n_e = -\rho_e/e$ (m^{-3}).

Figure 10: (colored) *Simulation 3.* Comparison of results at $T = 20ns$ with $\text{SGCC}_1^{1.5}$ and $\text{SGCC}_2^{1.5}$ schemes.

The peak field strength (on the symmetry axis) and the streamer length are presented in Figure 11. As Simulation 2, the SG scheme is always too diffusive that it provides inadequate results. On $\Delta z = 1.5\mu m$ grid it crashes at $T = 10ns$, while on $\Delta z = 0.8\mu m$ it overestimates the streamer velocity (Figure 11c) and the peak field strength (Figure 11d) that the streamer already touches the cathode at $T = 20ns$. On Figure 11a SGCC_2^3 is comparable to $\text{SGCC}_1^{1.5}$ and $\text{MUSCL}^{1.5}$; $\text{SGCC}_2^{1.5}$ is roughly the same as $\text{SGCC}_1^{0.8}$ and $\text{MUSCL}^{0.8}$; only $\text{SGCC}_2^{0.8}$ is comparable to the CWI reference curve. The FR reference curve seems to be less accurate since it underestimates the streamer velocity. On Figure 11b we observe that the aforementioned oscillations pollute the results of SGCC_2^3, $\text{SGCC}_1^{1.5}$ and $\text{MUSCL}^{1.5}$, all these three curves are more or less the same; $\text{SGCC}_2^{1.5}$, $\text{SGCC}_1^{0.8}$ and $\text{MUSCL}^{0.8}$ form a cluster with the FR reference curve; only $\text{SGCC}_2^{0.8}$ manages to reach the accuracy of CWI. We also observe a chute of peak field from $230kVcm^{-1}$ at the end of streamer formation to $190kVcm^{-1}$ on a length of $70mm$, which contradicts the stable quasi-constant field observed in Simulation 2. Indeed, the streamer decays more easily in this situation since the pre-ionized electron level is lower, hence limits to capability of charge production by ionization avalanches to maintain the streamer front. Overall, for the same quality of results, the SGCC_2 scheme allows the use of grids twice as coarse as SGCC_1 and MUSCL.

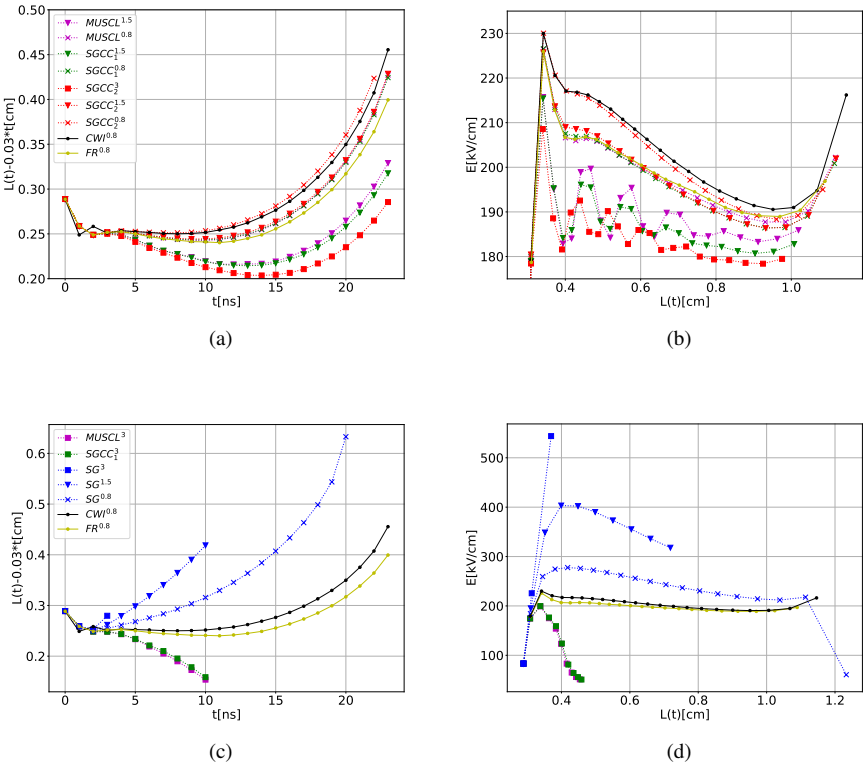

Figure 11: (colored) *Simulation 3.* Amplified streamer length $L - vt$ (cm) versus time with $v = 0.03cm.s^{-1}$ (left) and peak field strength $E_{\max}$ $(kVcm^{-1})$ versus streamer length (right). Reference curves in black and yellow.

7. Conclusion and perspectives

This section concludes the introduction of the Scharfetter-Gummel schemes with Correction of Current. The SGCC method offers a consistent tool to discretize the second-order operator $\partial_x - \partial^2_{xx}$ without having to discretize the convective and diffusive parts separately. The key idea is to find a p-degree polynomial approximation of the density flux such that it is locally and quasi exact for an exponential function. The construction of the schemes can be finally viewed as a correcting process of the classical Scharfetter-Gummel scheme, with the corrections from the spatial derivatives of the solution. Thus to close the numerical flux, approximations of the solution derivatives must be chosen carefully.

For $p = 1$, analysis has shown that the integration of classical TVD limiters into the SGCC method results in stable schemes in the sense that the numerical solution respects the discrete maximum and TVD properties. For $p = 2$, we have applied the generalized moment limiting method to approximate the solution derivatives. Although, to our knowledge, no theoretical results have demonstrated that this method is

stable, numerical results have shown that the scheme is highly accurate and sufficiently robust to simulate plasma discharge in air on structured meshes. The results of $SGCC_2$ on coarse grids are of the same quality as second-order schemes on more refined grids. This is a practical interest of this scheme since it eases computational burdens.

In the future, we aim to extend and apply the SGCC method on unstructured grids and we hope to combine the SGCC framework with stable solution reconstruction routines to achieve higher accuracy.

Acknowledgments

The present work is funded by The French Aerospace Lab and the Université Toulouse 3-Paul Sabatier in the framework of the PhD scholarship of N. Tuan Dung.

The authors thank Guillaume Dufour (The French Aerospace Lab, France) for his help with the implementation of the algorithms.

References

[1] D. L. Scharfetter, H. K. Gummel, Large-signal analysis of a silicon read diode oscillator, IEEE Transactions on electron devices 16 (1969) 64–77.

[2] R. Eymard, T. Gallouët, R. Herbin, Finite volume methods, Handbook of numerical analysis 7 (2000) 713–1018.

[3] B. Van Leer, Towards the ultimate conservative difference scheme i. the quest of monotonicity, in: Proceedings of the Third International Conference on Numerical Methods in Fluid Mechanics, Springer, 1973, pp. 163–168.

[4] B. Van Leer, Towards the ultimate conservative difference scheme. ii. monotonicity and conservation combined in a second-order scheme, Journal of computational physics 14 (1974) 361–370.

[5] B. Van Leer, Towards the ultimate conservative difference scheme iii. upstream-centered finite-difference schemes for ideal compressible flow, Journal of Computational Physics 23 (1977) 263–275.

[6] B. Van Leer, Towards the ultimate conservative difference scheme. iv. a new approach to numerical convection, Journal of computational physics 23 (1977) 276–299.

[7] B. Van Leer, Towards the ultimate conservative difference scheme. v. a second-order sequel to godunov's method, Journal of computational Physics 32 (1979) 101–136.

[8] P. K. Sweby, High resolution schemes using flux limiters for hyperbolic conservation laws, SIAM journal on numerical analysis 21 (1984) 995–1011.

[9] A. Harten, High resolution schemes for hyperbolic conservation laws, Journal of computational physics 135 (1997) 260–278.

[10] P. Colella, P. R. Woodward, The piecewise parabolic method (ppm) for gas-dynamical simulations, Journal of computational physics 54 (1984) 174–201.

[11] A. Harten, S. Osher, Uniformly high-order accurate nonoscillatory schemes. i, SIAM Journal on Numerical Analysis (1987) 279–309.

[12] A. Harten, B. Engquist, S. Osher, S. R. Chakravarthy, Uniformly high order accurate essentially non-oscillatory schemes, iii, in: Upwind and high-resolution schemes, Springer, 1987, pp. 218–290.

[13] C.-W. Shu, Essentially non-oscillatory and weighted essentially non-oscillatory schemes for hyperbolic conservation laws, in: Advanced numerical approximation of nonlinear hyperbolic equations, Springer, 1998, pp. 325–432.

[14] T. J. Barth, Aspects of unstructured grids and finite-volume solvers for the euler and navier-stokes equations, AGARD, Special Course on Unstructured Grid Methods for Advection Dominated Flows (1992).

[15] F. Haider, P. Brenner, B. Courbet, J.-P. Croisille, Efficient implementation of high order reconstruction in finite volume methods, in: Finite Volumes for Complex Applications VI Problems & Perspectives, Springer, 2011, pp. 553–560.

[16] M. Yang, Z.-J. Wang, A parameter-free generalized moment limiter for high-order methods on unstructured grids, in: 47th AIAA Aerospace Sciences Meeting Including The New Horizons Forum and Aerospace Exposition, 2009, p. 605.

[17] S. Clain, S. Diot, R. Loubère, A high-order finite volume method for systems of conservation laws—multi-dimensional optimal order detection (mood), Journal of computational Physics 230 (2011) 4028–4050.

[18] C. Ollivier-Gooch, M. Van Altena, A high-order-accurate unstructured mesh finite-volume scheme for the advection–diffusion equation, Journal of Computational Physics 181 (2002) 729–752.

[19] D. de G. Allen, R. Southwell, Relaxation methods applied to determine the motion, in two dimensions, of a viscous fluid past a fixed cylinder, The Quarterly Journal of Mechanics and Applied Mathematics 8 (1955) 129–145.

[20] A. M. Il'in, Differencing scheme for a differential equation with a small parameter affecting the highest derivative, Mathematical Notes of the Academy of Sciences of the USSR 6 (1969) 596–602.

[21] H.-G. Roos, M. Stynes, L. Tobiska, Robust numerical methods for singularly perturbed differential equations: convection-diffusion-reaction and flow problems, volume 24, Springer Science & Business Media, 2008.

[22] E. C. Gartland, Uniform high-order difference schemes for a singularly perturbed two-point boundary value problem, Mathematics of computation 48 (1987) 551–564.

[23] L. Liu, J. van Dijk, J. ten Thije Boonkkamp, D. B. Mihailova, J. J. van der Mullen, The complete flux scheme—error analysis and application to plasma simulation, Journal of Computational and Applied Mathematics 250 (2013) 229–243.

[24] P. A. Markowich, C. A. Ringhofer, S. Selberherr, M. Lentini, A singular perturbation approach for the analysis of the fundamental semiconductor equations, IEEE Transactions on Electron Devices 30 (1983) 1165–1180.

[25] M. Chatard, Asymptotic behavior of the scharfetter–gummel scheme for the drift-diffusion model, in: Finite Volumes for Complex Applications VI Problems & Perspectives, Springer, 2011, pp. 235–243.

[26] M. Bessemoulin-Chatard, C. Chainais-Hillairet, M.-H. Vignal, Study of a finite volume scheme for the drift-diffusion system. asymptotic behavior in the quasi-neutral limit, SIAM Journal on Numerical Analysis 52 (2014) 1666–1691.

[27] R. Eymard, J. Fuhrmann, K. Gärtner, A finite volume scheme for nonlinear parabolic equations derived from one-dimensional local dirichlet problems, Numerische Mathematik 102 (2006) 463–495.

[28] M. Bessemoulin-Chatard, A finite volume scheme for convection–diffusion equations with nonlinear diffusion derived from the scharfetter–gummel scheme, Numerische Mathematik 121 (2012) 637–670.

[29] M. Patriarca, P. Farrell, J. Fuhrmann, T. Koprucki, Highly accurate quadrature-based scharfetter–gummel schemes for charge transport in degenerate semiconductors, Computer Physics Communications 235 (2019) 40–49.

[30] C. Chainais-Hillairet, Y.-J. Peng, Convergence of a finite-volume scheme for the drift–diffusion equations in 1d, IMA journal of numerical analysis 23 (2003) 81–108.

[31] C. Chainais-Hillairet, J.-G. Liu, Y.-J. Peng, Finite volume scheme for multi-dimensional drift-diffusion equations and convergence analysis, ESAIM: Mathematical Modelling and Numerical Analysis 37 (2003) 319–338.

[32] C. Chainais-Hillairet, Y.-J. Peng, Finite volume approximation for degenerate drift-diffusion system in several space dimensions, Mathematical Models and Methods in Applied Sciences 14 (2004) 461–481.

[33] M. Bessemoulin-Chatard, F. Filbet, A finite volume scheme for nonlinear degenerate parabolic equations, SIAM Journal on Scientific Computing 34 (2012) B559–B583.

[34] J. Boeuf, Y. Lagmich, T. Unfer, T. Callegari, L. Pitchford, Electrohydrodynamic force in dielectric barrier discharge plasma actuators, Journal of Physics D: Applied Physics 40 (2007) 652.

[35] G. Dufour, F. Rogier, Numerical modeling of dielectric barrier discharge based plasma actuators for flow control: the copaier/cedre example, Aerospace Lab (2015).

[36] J. Matéo-Vélez, P. Degond, F. Rogier, A. Séraudie, F. Thivet, Modelling wire-to-wire corona discharge action on aerodynamics and comparison with experiment, Journal of Physics D: Applied Physics 41 (2008) 035205.

[37] Y. Zhu, Y. Wu, B. Wei, H. Xu, H. Liang, M. Jia, H. Song, Y. Li, Nanosecond-pulsed dielectric barrier discharge-based plasma-assisted anti-icing: modeling and mechanism analysis, Journal of Physics D: Applied Physics 53 (2020) 145205.

[38] O. Eichwald, H. Bensaad, O. Ducasse, M. Yousfi, Effects of numerical and physical anisotropic diffusion on branching phenomena of negative-streamer dynamics, Journal of Physics D: Applied Physics 45 (2012) 385203.

[39] J. Teunissen, U. Ebert, Simulating streamer discharges in 3d with the parallel adaptive afivo framework, Journal of Physics D: Applied Physics 50 (2017) 474001.

[40] J. ten Thije Boonkkamp, M. Anthonissen, The finite volume-complete flux scheme for advection-diffusion-reaction equations, Journal of Scientific Computing 46 (2011) 47–70.

[41] A. Kulikovsky, A more accurate scharfetter-gummel algorithm of electron transport for semiconductor and gas discharge simulation, Journal of computational physics 119 (1995) 149–155.

[42] A. Kulikovsky, Positive streamer between parallel plate electrodes in atmospheric pressure air, Journal of physics D: Applied physics 30 (1997) 441.

[43] A. Kulikovsky, Positive streamer in a weak field in air: A moving avalanche-to-streamer transition, Physical Review E 57 (1998) 7066.

[44] R. J. LeVeque, R. J. Leveque, Numerical methods for conservation laws, volume 132, Springer, 1992.

[45] S. Gottlieb, C.-W. Shu, E. Tadmor, Strong stability-preserving high-order time discretization methods, SIAM review 43 (2001) 89–112.

[46] G. Hagelaar, L. Pitchford, Solving the boltzmann equation to obtain electron transport coefficients and rate coefficients for fluid models, Plasma Sources Science and Technology 14 (2005) 722.

[47] N. Sato, Discharge current induced by the motion of charged particles, Journal of Physics D: Applied Physics 13 (1980) L3.

[48] B. Bagheri, J. Teunissen, U. Ebert, M. M. Becker, S. Chen, O. Ducasse, O. Eichwald, D. Loffhagen, A. Luque, D. Mihailova, et al., Comparison of six simulation codes for positive streamers in air, Plasma Sources Science and Technology 27 (2018) 095002.

[49] R. Morrow, J. Lowke, Streamer propagation in air, Journal of Physics D: Applied Physics 30 (1997) 614.

[50] Y. P. Raizer, J. E. Allen, Gas discharge physics, volume 2, Springer Berlin, 1997.

[51] G. Strang, On the construction and comparison of difference schemes, SIAM journal on numerical analysis 5 (1968) 506–517.

[52] S. Celestin, Study of the dynamics of streamers in air at atmospheric pressure, Ph.D. thesis, Ecole Centrale Paris, 2008.